EUROPEAN ORGANIZATION FOR NUCLEAR RESEARCH

CERN-EP/82-83
25 June 1982

# PROGRESS IN CHERENKOV RING IMAGING: PART 1. DETECTION AND LOCALIZATION OF PHOTONS WITH THE MULTISTEP PROPORTIONAL CHAMBER

R. Bouclier, G. Charpak, A. Cattai, J. Million,
A. Peisert, J.C. Santiard and F. Sauli

CERN, Geneva, Switzerland

G. Coutrakon, J.R. Hubbard, Ph. Mangeot,
J. Mullie and J. Tichit

CEN, Saclay, France

H. Glass, J. Kirz and R. McCarthy

State Univ. of New York, Stony Brook, NY, USA

## ABSTRACT

The multistep proportional chamber, operated with a photosensitive gas filling, makes it possible to obtain stable multiplication factors in excess of $10^6$ and can be used for the detection of single photoelectrons released in the gas. The efficiency and localization properties of the device in the detection of vacuum ultraviolet photons are discussed here, in view of its use for particle identification exploiting the Cherenkov ring-imaging method.

(Submitted to Nuclear Instruments and Methods in Physics Research)

## 1. INTRODUCTION

Cherenkov ring imaging using multiwire proportional gas counters as photon detectors was introduced several years ago as a very promising technique for particle identification at high energies [1]. Various methods for photon detection and localization have since been devised and are described in the literature; for a complete bibliography see, for example, Coutrakon et al. [2]. Two major problems confront the experimenter in this field. On the one hand, the high-frequency cut-off of the best vacuum ultraviolet windows demands the use in the detector of photo-ionizing vapours with the lowest possible ionization potential, generally of rather delicate manipulation. Moreover, electronic detection of single photoelectrons in a gaseous counter requires stable and large multiplication factors, of $10^6$ or so, to be attained and this in a gas mixture that, because of its intrinsic large photosensitivity, is particularly prone to secondary processes.

In the course of the development of a large Cherenkov ring-imaging device for experiment E605 at Fermilab, we have built and tested various configurations of photon detectors and studied extensively their localization properties. Most of these measurements have been realized using a multistep proportional chamber as detector, and triethylamine (TEA) as the photo-ionizing vapour in addition to a noble gas carrier; the main results of our investigation are described here. In a separate paper, we will describe the beam test of a ring-imaging detector prototype and its particle-localization properties [2]. The reasons for our choice of TEA as against the possibility of using even lower ionization potential vapours [such as tetrakis(dimethylamine)ethylene (TMAE)] are also discussed there.

## 2. AVALANCHE-SIZE DISTRIBUTION GENERATED BY SINGLE ELECTRONS IN PROPORTIONAL COUNTERS

The avalanche multiplication characteristics of gaseous proportional counters in the detection of single photoelectrons have been the subject of extensive research, both from the theoretical and the experimental standpoint. Knowledge of the fluctuations in the size of avalanches started by one electron is indeed essential in order to estimate the limiting energy resolution of proportional counters

(see for example Curran and Craggs [3]). In a uniform field geometry, and assuming that each electron has a constant probability of undergoing ionizing collisions, simple probability considerations allow the computation of the following experimental avalanche-size distribution [4]:

$$P(n) \simeq \frac{1}{\bar{n}} e^{-n/\bar{n}} , \qquad (1)$$

where $\bar{n}$ is the average value of the avalanche size. The expression implies that the maximum probability corresponds to no multiplication at all. Such a pulse-height distribution is indeed observed at moderate multiplication factors. At high gains, however, the experimental distribution ceases to be exponentially decreasing and develops a distinct peak around the average with a consequent reduction of its variance [3]. It appears that the shape of the distribution depends more on the field strength (and therefore on the value of the first Townsend coefficient) than on the total gain, proving that the peak is not a space-charge-related effect; this is apparent in Fig. 1, where the pulse-height distributions for avalanches generated by single electrons in methylal are measured at increasing values of field, but at correspondingly smaller values of the gap so as to keep the effective total charge roughly constant [5].

Several theoretical models have been proposed to explain the observed avalanche-size distribution at high fields [6-9]. They generally agree in suggesting a functional form of the Polya type with one parameter b:

$$P(n) = \frac{b^b}{\bar{n}\Gamma(b)} \left(\frac{n}{\bar{n}}\right)^{b-1} e^{-b(n/\bar{n})} \qquad (2)$$

that reduces to the exponential (1) for b = 1. Typical observed values of b at high gains vary between 1.5 and 2.

The practical implications of a peaked pulse-height distribution as compared to an exponential one are obvious. In the case where the counter's signals are simply discriminated and scaled, the appearance of a peak in the input pulses' distribution implies that for a low enough threshold setting a constant efficiency

plateau can be measured when increasing the operational voltage above the minimum for detection: this would not be the case for an exponentially decreasing pulse-height distribution. Examples of efficiency plateau obtained in the peaked condition will be shown in Section 5.1. Moreover, when using a centre-of-gravity read-out to improve the localization accuracy, a peaked distribution is useful since it limits the required dynamic range for the amplitude-measuring electronics and reduces the dispersions connected with gain linearity, uniformity, and signal pileups.

While a peaked avalanche distribution seems to be a general characteristic of high gains, this does not imply that one can reach these operational conditions in all gases; moreover, especially in photosensitive gas mixtures such as the ones we are interested in, various secondary processes connected with photon and ion feedback limit the gain to about $10^5$ or so before discharge sets in. For a single electron avalanche, this is somewhat at the lower edge of the amount of charge that can be handled by the simple and cheap electronic circuits currently used in the work on proportional chambers.

Larger stable gains can indeed be obtained in multiwire proportional chambers, sometimes in excess of $10^7$, by a careful choice of the gas mixture that normally includes photon-absorbing hydrocarbons and electronegative vapours for an effective quenching of secondary processes leading to discharge [10]. Such an approach is obviously not possible when the goal is to preserve good quantum efficiency in a wavelength interval as large as possible.

Operating a conventional multiwire proportional chamber with various concentrations of photosensitive vapours added to noble gases, we have identified two main mechanisms that limit the stable gain to values around $10^5$. The first effect, which appears when using a few per cent of TEA in argon or helium, is the onset of a typical Geiger discharge propagating along the anode wires irradiated and sometimes extending across several adjacent wires. Indeed, one expects this to happen in a gas where the mean free path for photoelectric absorption of photons, emitted in the avalanches in the energy domain where the additive has large quantum efficiency,

is around 1 mm*). As an example, Fig. 2 shows the transition from proportional to Geiger regimes observed in a multiwire proportional chamber with 2 mm wire spacing, operated with 2% TEA in helium. The maximum proportional gain is limited to about $10^5$, and the transition is observed when increasing the anodic voltage by a few tens of volts.

Use in a proportional chamber of photosensitive vapours having much lower vapour pressure, such as TMAE, leads to a different secondary process. Because of their long range in the gas, several centimetres or so, ultraviolet photons emitted in the avalanche can reconvert rather far from the origin or can reach the surrounding electrode and extract there secondary electrons; a second avalanche develops in this case at a well-defined time interval (the time it takes for the electrons to drift back to the anode). An example is shown in Fig. 3, as observed in a chamber operated with 1% TMAE in argon at gains slightly in excess of $10^4$. Increasing the gain further, new generations of secondary avalanches appear and very quickly a diverging condition is reached leading to discharge. Such a behaviour is perhaps more insidious than the previous one, since it leads to spurious avalanches well separated spatially from the primary thus spoiling the localization properties of the detector or increasing its rate of accidentals. Only recently, by a careful design of the detector geometry and using pure methane, instead of a noble gas, gains in excess of $10^5$ have been recorded using TMAE as the photo-ionizing agent [11].

The problems quoted have frustrated most early attempts to use conventional multiwire proportional chambers for efficient detection of ultraviolet photons. During the development of the multistep proportional chamber [12] it was observed that separation of the overall amplification process into two distinct elements, each well below the critical region, allowed large stable gains, of $10^6$ or more, to be attained in photosensitive gas mixtures, thus permitting efficient detection

---

*) The total absorption cross-section of TEA is about 20 Mb at 1450 Å, which implies a 1 mm absorption length for 2% TEA at that wavelength.

of single photoelectrons. The first Cherenkov ring images in a gaseous detectors were indeed observed using a multistep device [13].

## 3. THE MULTISTEP PROPORTIONAL CHAMBER AS A PHOTON DETECTOR

The operational principle and the properties of multistep proportional chambers have been described extensively elsewhere [12-16] and only a brief summary will be given here.

Under the action of a strong uniform field between two electrodes, electrons experience various inelastic processes leading to the growth of an avalanche. For some gas mixtures, mainly the ones containing a pure noble gas with the addition of a little alcohol, acetone, or other organic vapours, the avalanche spreads spatially during the growth more than would be expected from the low-field electron diffusion coefficients in the given gas mixture; typically, in a 4 mm gap operated with 1% acetone in argon at a gain around $10^4$, the front of the electron avalanche has a width of around 2 mm FWHM. As the ionization potential of the quoted additives is generally smaller than the excitation potential of the noble gas and of the energy of photons emitted by secondary scintillation, either a photon-propagated avalanche spread or a Penning-type diffusion mechanism have been suggested as being responsible for the observed spread [12-15]. One practical consequence of the large avalanche extension is, however, that the electric field in a multielectrode structure can be arranged in such a way as to transfer a uniform fraction of the electron avalanche into a subsequent element. A schema of the electrode configuration in a multistep chamber is shown in Fig. 4. A region of moderate electric field, named conversion or drift space, is separated by a wire mesh from a region where higher fields can be applied in a parallel-plate geometry, the so-called preamplification space. Electrons produced within the conversion space by an ionizing event drift towards and into the high field region where they multiply in an avalanche process. Electrons in the avalanche located within the field-line tubes connecting the preamplification region to the lower field transfer region are injected there and proceed towards the following amplification element, a conventional multiwire proportional chamber as in the drawing.

A typical distribution of electron charge as measured for an avalanche developing in a 4 mm thick gap in a mixture of 0.5% TEA in argon is shown in Fig. 5 [17], and has a Gaussian shape with a standard deviation of 800 μm. In Fig. 6, the measured r.m.s. of the avalanche width in the same geometry is plotted as a function of the TEA concentration in argon. Somewhat smaller spreads have been observed in mixtures of TEA with helium (see Section 5.3), but a systematic measurement of avalanche size in this case has not been made.

As far as the transverse avalanche spread in the preamplification region is comparable with the pitch of the wires constituting the transfer grid, the charge-transfer efficiency has only a little dependence on the average position of the original avalanche and equals roughly the ratio between the transfer and preamplification field strengths. Figure 7 shows, for example, the computed transfer efficiency for several avalanche sizes, as a function of average position and for a wire mesh having 500 μm pitch. Clearly, for avalanches having 200 μm r.m.s. or more, the transfer efficiency is almost independent of the position.

The fraction of electrons drifting in the transfer region enters into the second amplification element, a conventional multiwire proportional chamber, see Fig. 4; as the field there is generally higher, almost all charge is transferred. It was observed in the early works on the multistep chamber that in the double structure one could reach safely overall amplifications largely exceeding the ones that could be obtained in a single device when operated with a photosensitive gas mixture. As an example, Fig. 8 shows the pulse-height distributions for single photoelectrons, as measured in a multistep proportional chamber operated with 1.5% TEA in argon at increasing values of the overall gain [17]; the amplitude scale is given in terms of detected charge on the anode wires (1 pC corresponds to a charge gain of about $6 \times 10^6$ in the detector). The peaked structure of the distribution typical of large gains is apparent, as discussed in the previous section.

In such a structure full detection efficiency for single electrons can be achieved with relatively low sensitivity electronics, and localization by the

centre-of-gravity method is greatly facilitated by the peaked signals with reduced dynamic range (see Section 5).

## 4. CONSTRUCTION AND TESTING OF THE PHOTON DETECTOR

### 4.1 The multistep proportional chamber

We have built and tested several prototype photon detectors based on the multistep proportional chamber principle. Most of the results described here have been obtained with a detector which has an active area of 200 × 200 $mm^2$ and whose major parameters are listed in Table 1 (which refers to Fig. 4). For the actual Cherenkov ring imager, described in Ref. 2, some parameters have been slightly modified, as for example the multiwire proportional chamber gap thickness, which was reduced to 3.2 mm to improve the separation of adjacent clusters. A set of machined fibre-glass frames, holding the various electrodes, are stacked and held together with a conventional O-rings and bolting system, see Fig. 9. A ribbed aluminium frame on one side, and the calcium fluoride window mount on the other side ensure the necessary rigidity of the structure. To eliminate the possibility of water vapour permeation the gas of the detector, which could affect its quantum efficiency, a double mylar window configuration has been adopted with the outgoing gas from the active volume flowing in the interface between the two sheets before the exhaust.

All passive electrodes, i.e. without readout electronics, are implemented with a stainless steel mesh having crossed wires 50 μm thick at 500 μm pitch. The meshes are stretched over the frames and soldered on suitable copperized-board insets; electrical contact is provided by extensions of the board itself.

The multiwire proportional chamber consists of three meshes of parallel wires; copper-beryllium wires 50 μm in diameter and 1.27 mm apart for the cathodes, and gold-plated tungsten wires, 20 μm in diameter with 2 mm spacing for the anode plane. The two cathode planes are perpendicular to each other, and the anode wires mounted at 45° to the cathode. Although each wire output is accessible on a multipin connector for testing purposes, for most of the measurements four adjacent cathode

wires are grouped together on each measuring channel, constituting strips about 5 mm wide. The anodes, on the other hand, are read out individually.

The wire orientation chosen ensures a redundant measurement of the coordinates for each point, thus partly overcoming the ambiguous coordinate coupling in the case of several close and simultaneous points (see below).

The construction of the preamplification gap deserves particular mention. Since one wants to attain here very high values of electric field in a parallel-plate geometry, precautions against edge breakdown have to be taken. We have experimented with various configurations that help to prevent the spontaneous breakdown at the frame edges before reaching a useful preamplification gain. The more effective geometries are shown in the insets of Fig. 29. In inset (a) two thin insulating strips have been inserted on each side of the gap, in close contact with the electrodes; 100 μm thick mylar or kapton strips, extending 4-5 mm into the gap, appear to be sufficient to prevent edge breakdown up to very high fields, probably just because they more than double the possible conduction channels on the frame surface. A more effective protection is given, however, by the geometry shown, as well as in inset (b), in the complete cross-section, that provides a physical increase of the gap thickness at the edge when the chamber is assembled. A specially machined fibre-glass frame, the "pusher", has insulating extrusions that reduce the gap thickness upon tightening the chamber by squeezing down the upper grid all around its edges. A reduction of 1/3 to 1/4 of the original gap appears sufficient to allow the highest fields to be reached without edge breakdown. Although mechanically more difficult to implement, this solution gave the more reproducible results and should be preferred whenever possible.

Because of its parallel-plate geometry, the preamplification element has a rather critical gain dependence on the gap thickness and uniformity of the electrodes. It has been computed, and experimentally verified, that the gain variation due to a decrease $\delta$ in the gap thickness $\ell$ can be expressed by [15]:

$$M(\ell - \delta) = M(\ell)\ e^{k\delta}, \quad M(\ell) = e^{\alpha\ell}, \tag{3}$$

where k is a gas constant describing the slope of the first Townsend coefficient $\alpha$ at increasing fields, in a local linear approximation:

$$\alpha(E) \simeq AE - k \ . \qquad (4)$$

We have measured the amplification factor, for a 4 mm thick gap, in a helium-triethylamine mixture (1.5% TEA in helium), see Fig. 10. The slope parameter k, taken from expression (4) is about 8.1 $mm^{-1}$ at the higher gains; from expression (3), therefore, one can see that a gain increase by a factor of two is obtained for a reduction of 90 μm in the 4 mm gap. While a 40-50 μm gap tolerance is not difficult to achieve in a small detector, like the one described here, both mechanical non-uniformities and electrostatic gap distortions are increasingly hard to control in large detectors and some gap-restoring or support-line device has to be envisaged with a geometry similar to the one adopted at the frame's edge.

4.2 Construction of the calcium fluoride windows

Detection of photons in the vacuum ultraviolet domain (VUV) requires the use of a fluoride crystal window. Despite its lower cut-off (about 10 eV) we have preferred calcium to lithium fluoride because of the stability in transmission characteristics that are not degraded by prolonged exposure to the atmosphere. Calcium-fluoride crystals with VUV transmission properties can be purchased up to large diameters, about 270 mm*); in the perspective, however, of having to build a larger surface detector, we have preferred to experiment with smaller crystals mounted on a support frame, a solution that turns out to be cheaper for a given surface. To cover the 200 × 200 $mm^2$ active area of the detector, we have used four 4 mm thick crystals and tried several methods of mounting on a support that has the necessary stiffness to withstand the mechanical stresses and introducing a minimum dead space for photon transmission. A first attempt, based on the use of conventional rubber O-rings compressed on the crystal edges by tiny bars (Fig. 11a), gave rather poor results in terms of gas-tightness and also presented

*) Produced by Harshaw Chemical Co., Solon, Ohio, USA.

severe problems of electrical insulation between the metal support bars and the first mesh in the detector (that has the highest potential in the chamber). Directly glueing the crystals on the support frame, Fig. 11b, was more satisfactory and indeed most of the results described in the next section and in Ref. 2 were obtained using a composite window of this kind. The choice of the glue has, however, to satisfy somewhat conflicting requirements. Because of the different thermal-expansion coefficients of the crystal and of the support, the coupling should have sufficient elasticity to avoid the buildup of excessive stresses; on the other hand, the purity requirements of the radiator side in the ring-imaging set-up demand a very small outgassing of all materials employed. It appears that most vacuum-grade epoxies (such as for example Torr Seal*) and Epotek**) have a very high grade of hardness and their use has resulted in localized or extended cleavage of the crystals. A limited success was obtained using a softer two-component silicon compound***), which has the desired mechanical characteristics to avoid local stresses but appeared in the long range to be permeable to TEA thus partly spoiling the purity of the gas in the Cherenkov radiator.

The last mounting scheme, Fig. 11c, seems to have solved the above-mentioned problems. Each individual window is first glued along its edges to a thin (0.1 mm) stainless steel square-shaped tube, which has a size slightly exceeding the perimeter of the crystal. The framed elements are then glued into a supporting frame that has suitable grooves as shown in the figure. Both bondings are realized with vacuum-grade epoxy, thus ensuring a very low outgassing and no permeation to foreign molecules. The tensional stress due to temperature variations is thus avoided by the flexible coupling; indeed, part of the curing process requires a temperature above 100 °C to be reached without damage to the crystals. The picture of an assembled four-crystal window, before being mounted on the detector, is shown in Fig. 12. For structural reasons, the main cross-like support is

---

*) Torr Seal, produced by Varian Vacuum Division, Polo Alfo, Calif., USA.

**) Epotek H77, produced by Epoxy Technology Inc., Billerica, Mass., USA.

***) $CAF_4$, produced by Rhone Poulenc, Div. Silicones, Paris, France.

machined out of a brass sheet; because of the way the crystals are mounted, however, it is not possible to electrically insulate the support from the first mesh in the detector. The metal frame is therefore glued to an insulating fibre-glass frame, visible in the picture, that can then bolted to the radiator body with a teflon separation frame that ensures the insulation.

### 4.3 A vacuum ultraviolet timing photon source

For laboratory testing of the detector, and in order to study its localization properties, we have developed a VUV photon source exploiting the light-emission properties of noble gases excited by ionizing radiation. As schematically indicated in Fig. 13, a gas-tight insulating envelope with a $CaF_2$ window contains an $\alpha$-emitting source. A semitransparent mesh, mounted on the inside surface of the crystal, allows a difference of potential to be applied across the gas volume, the source holder being grounded. The presence of an electric field allows not only the ionization produced in each decay to be collected and detected, but also to increase largely the photon yield through a process of secondary scintillation. Even using very thin collimators, 100 μm or so wide, between the source and the chamber, average yields of several photons per disintegration can be realized. We have mostly used krypton at atmospheric pressure as a gas filling, since its secondary emission occurs in a broad peak centred at around 1450 Å [18] almost coinciding with the peak quantum efficiency of TEA [13,19]. The source assembly can be applied over the detector window, after evacuating a small cylindrical flange, which is sealed both on the window and on the source side by O-rings. Collimators can be introduced within this volume to study localization properties.

Because of the long lifetime of the excited states in krypton and of the collection time of the electrons in the source, the photon emission occurs on each disintegration over about 1 μs, preventing any study of the timing properties of the detector with this device. Efficiency measurements can instead be implemented by using the charge signal from the source in coincidence with the detector output; only relative efficiencies can be measured, however, unless the number of emitted photons is separately measured with a calibrated detector. With careful

outgassing of the source and keeping a small flow of gas in it (1 $cm^3$ or so per minute) we could achieve a sufficient long-term stability in the photon yield to allow a comparison of efficiency plateaux measured with various detector geometries and gas fillings.

### 4.4 Pulse-height recording and calibrations

Charges collected on each anode wire and on groups of cathodes are preamplified on the detector and transmitted, through coaxial or twisted pair cables, to linear receivers followed by gated charge-to-digital converters. From the resulting pulse-height distribution, after some corrections to be described, the coordinates are computed using a centre-of-gravity algorithm [20]. Various configurations of amplifiers and receivers have been tried; a basic requirement was that they be cheap and compact enough so as to allow their use in large quantities. The scheme that has been used for part of the measurements described here and for the prototype ring-imaging detector is shown in Fig. 14. It consists of a charge preamplifier with a twisted-pair differential output (Fig. 14a), followed by a linear differential receiver buffered for a low impedance output (Fig. 14b). Only the circuit used for the cathode channels is shown, which has a full dynamic range (about -4 V at the receivers' output) for positive input charges; the anode channels are identical in design, but use complementary transistors in the preamplifier and an attenuation network (shown in the inset) to compensate for a larger input charge. We have adopted for the charge preamplifiers an RC shaping constant of around 400 ns. The charge-to-digital converter's gating pulse is shorter than the input signal and overlaps with it so that the recorded charge corresponds to the integral of the input during the gate length. Such a configuration has been preferred to a peak-sensing converter since it allows the overall sensitivity of the system to be modified by changing the gate length. The relatively long decay constant of the amplifiers allows the charge measurement to be less dependent on the relative timing between signal and gating pulse; indeed in our application the photon absorption length in the conversion space, typically 2 mm, introduces a jitter of about 100 ns in the detection time.

The sensitivity of the system, from the input to the receiver's output (on 50 Ω), is 400 and 150 mV $pC^{-1}$ for the cathode and anode channels, respectively. With the typical sensitivities of commercial charge-to-digital converters, which is about 250 pC full scale, an average anodic input charge of 1 pC (see Fig. 8) is recorded roughly in the middle of the dynamic range for a 50 ns gate.

The average electronics noise of the chain referred to its input corresponds to about $10^{-2}$ pC r.m.s., and is small compared to the average detected charge. The preamplifiers are organized on printed-circuit boards by groups of eight, the individual cards being plugged into a multiple connector board distributing the wires' signals. The connection is direct for the grounded cathode-wire plane, while low-leak high-voltage capacitors mounted on the mother board couple the anode wires to the corresponding amplifiers. The operating voltage is provided to the anode wires through individual 1 MΩ protection resistors, all connected to a common HV bus on the card. Protection against overload or accidental breakdown at the input is provided by three fast-switching diodes; no damage to the circuit results from a 500 pF, 5 kV discharge at the input, which largely exceeds the expected overload in the case of spark breakdown in the detector.

At the receiver side, an analogue sum of signals over 24 adjacent channels is used for monitoring; it is used also to allow self-triggering of the detector when using a calibration source.

For digital recording of the charge, we have used commercial high-density CAMAC-based charge-to-digital converters*) connected to a small on-line computer**) for data handling and monitoring.

An assembled multistep proportional chamber complete with the preamplifiers' electronics, used for laboratory testing, is shown in Fig. 15. It has a $200 \times 200$ mm$^2$ active surface, with a composite $CaF_2$ window as described. With two orthogonal cathode planes having 5 mm wide strips readout (indeed, 4 wires at 1/20 of an inch grouped together), and anode wires with 2 mm spacing inclined at 45° and individual

---

*) LeCroy ADC type 2249 A.

**) Hewlett Packard HP 2100.

readout, the detector requires around 230 pulse-height measuring channels to be fully equipped.

To reduce the unit cost of the amplifiers, the channel gain is not individually adjusted to the required tolerance. Instead, we have used a software calibration procedure for the complete system, which compensates for the gain differences and long-term drifts in individual channels. At a conveniently low operational voltage, to avoid saturation, the detector is uniformly irradiated with a $^{55}Fe$ 5.9 keV X-ray source, and the pulse-height distributions are recorded using the receivers' analogue sum output as the triggering source. After pedestal subtraction, the pulse-height spectra on all measurement channels are plotted, under the restrictive condition that a single anode has a significative pulse height in order to avoid the charge-sharing events (see the next section) that would produce a poor pulse-height resolution. For the cathode strips, on which the pulse height is obviously position-dependent, only the channel containing the highest pulse height in the distribution in each event is plotted; this ensures a good enough energy resolution for both the anode and cathode channels (Fig. 16). Once the pulse-height spectra have been collected with sufficient statistics for all channels, the average pulse height on the 5.9 keV peak is taken as representative of the channel gain; this includes all sources of gain variation, from the chamber to the charge-to-digital converter. The table of gains thus compiled is then used as a calibration constant to reduce all channels' gains to the same normalized value. We have found that this procedure is reproducible and reduces the corrected channel-to-channel dispersion to 5% or less.

A convenient way of monitoring the residual positioning errors connected with all dispersions and non-linearities of the system is to plot, again for a uniform illumination of the detector with X-rays, the difference $\Delta$ between a measured coordinate, and the value of the same coordinate as computed from the two other measured projections; a plot of $\Delta y$ as a function of y is presented in Fig. 17. The projection of the distribution on the ordinate has a Gaussian shape with 250 μm r.m.s.; this represents the overall localization error due mostly to residual non-linearities, gain variations, and electronics noise.

One should remember that the centre-of-gravity localization procedure is not very sensitive to local gain variations; this is because the distribution is normalized to itself. In Fig. 18, we have simulated the effect of a 50% gain variation on one cathode channel, corresponding to the 5 mm wide strip centred around y = 56 mm. The oscillation that results has a maximum width of 1 mm; the positioning error due to a single-channel gain variation is therefore about 20 μm for each variation.

## 5. DETECTION AND LOCALIZATION OF VACUUM ULTRAVIOLET

### 5.1 Detection efficiency

We have used the timing VUV source described in Section 4.3 both to study the detection efficiency of the chamber and to analyse its localization properties. To perform the first kind of measurement, the analogue summing output from an anode receiver is applied to a fast discriminator with adjustable threshold. The detector efficiency is then defined as the ratio between the number of discriminated pulses in coincidence with the timing trigger provided by the source and the number of triggers. This is of course a relative measurement, containing no information about the absolute quantum efficiency of the device. However, adjusting the source voltage and collimation so as to measure a plateau with typically 20% detection efficiency, one can make sure that the results correspond to the detection of a single photoelectron. Indeed, for a Poisson-like distribution in the number of detected photons, at the quoted total-efficiency level the number of events with two or more simultaneous photons is about 2%. This argument holds only if a constant efficiency plateau is found at increasing gain of the chamber; this is indeed the case for a gas filling containing 1.5% TEA in helium, as shown in Fig. 19. The relative efficiency is given as a function of the anodic voltage, and for three values of the preamplification gap voltage; the transfer potential, HV3 in Fig. 4, was kept constant and equal to -1 kV. The discrimination threshold was set at 0.1 pC, which is comfortably higher than the electronics noise and corresponds to about $5 \times 10^5$ electrons (see also Fig. 8). Essentially the same behaviour is observed when adding a small quantity of methane to the mixture, although the working potentials are slightly higher (Fig. 20).

Both quoted measurements were obtained by keeping a constant drift field in the conversion gap, about 1 kV $cm^{-1}$; it is interesting, however, to look at the behaviour of the relative efficiency at fixed gain, as a function of the drift potential (Fig. 21). After a sudden increase above zero field, where electron collection begins, there is an indication of a slight increase of efficiency over several hundred volts until a plateau is reached at around 600 V (1 kV $cm^{-1}$ in the 6 mm thick conversion gap). This may be an indication of either a slight electronegativity of the gas mixture, decreasing at high fields, or of a poor collection from the region between the first mesh and the window at low fields.

## 5.2 Pulse-height correlation and cluster size

Using a timing VUV photon source and the complete charge-recording system, we have studied the pulse-height and cluster-size distribution on anode wires and cathode strips. For each event, and after the pedestal subtraction and gain correction as described, the sum of recorded charges for the cluster of cathode-induced signals is computed, as well as the total anodic charge (because of charge interpolation, see below, a large fraction of the event interests two adjacent anode wires). A typical integrated cathode charge spectra, for a single photoelectron, is shown in Fig. 22.

Owing to the extended dynamic range of the detected charge, a fraction of the events (about 2%) contains one or more channels exceeding the linear range of the converters; for these saturated events an improved centre-of-gravity algorithm has been developed.

Because they originate in the same physical process, there is a correlation between the integral anode and cathode charges, as shown in Figs. 23 and 24 for the cathode vs cathode and cathode vs anode total detected charges, respectively. The correlation can be exploited to recognize correctly the triplet of clusters corresponding to each detected photon in the case of multiple events with ambiguous geometrical correlations. The relative amplitude difference between the two cathodes has a width of 5% FWHM (see Fig. 25).

Another powerful constraint used to disentangle spatially close events is given by the knowledge of the width of the induced cluster. Figure 26 shows the normalized charge distribution around the computed centre of gravity, for a large number of events; the distribution is very well represented by a Gaussian with a FWHM of 8 mm (or two cathode strips width). In the case of two close photons, partly overlapping in one projection, a fit with two Gaussian functions of known width (four free parameters) provides a good reconstruction of the original event, see Fig. 27. For the event in the figure, the distance between the two photons in the projection is about 8 mm.

The double-cluster resolution is obviously a function of the gap thickness in the MWPC, which is 5 mm for the chamber described here; to improve this parameter, we have reduced the gap to 3.2 mm in the finally adopted geometry of the Cherenkov ring-imaging detector.

### 5.3 Localization accuracy

Using a narrow slit collimator on the photon source, we have recorded and analysed the centre-of-gravity distributions for various relative orientations between the source and the detector. Indeed, while one expects a uniform dependence of the centre of gravity on the real position for the coordinate measured in the direction parallel to the anode wires, for the perpendicular direction the quantizing effect of the anodes normally leads to discrete values corresponding to the wire spacing. In the multistep detector, however, as described in Section 3, the lateral spread of the avalanche in the preamplification element results for most events in a charge sharing between two or more adjacent anodes with, as a consequence, an effective coordinate interpolation.

Measurements of avalanche size as a function of the TEA concentration in argon were given in Fig. 6; in order, however, to estimate the probability of charge sharing, one has to take into account the detailed mechanism of the mutual signal induction between adjacent anode wires. In the MWPC geometry of our detector, the positive signal induced on the neighbouring wires by an avalanche developing around a given anode represents about 10% of the main signal, however with

opposite sign thus partly cancelling the signal due to the original shared charge. In Fig. 28 we show the computed probability of charge sharing, i.e. the relative number of events resulting in two adjacent anodes with significative (negative) pulse height, as a function of the physical avalanche size and for a uniform exposure of the detector to the source. With reference to Fig. 6, in a 1.5% concentration of TEA in argon, the avalanche has about 600 μm r.m.s., and this results in roughly 80% of the events being of the charge-interpolating kind, as indeed observed for a uniform illumination of the detector with the photon source. The effect is very obvious when plotting the centre-of-gravity distribution with the source collimated in the direction perpendicular to the anodes (Fig. 29a). The distribution is indeed relatively uniform, the small oscillations being due to various geometrical shadows within the source collimation (owing, for example, to photon absorption in the grids); in the absence of charge interpolation, the distribution would appear as a succession of peaks 2 mm apart (for comparison, see Fig. 32). A projection of the distribution in the direction parallel to the anode wires is shown in Fig. 29b; it has a standard deviation of about 450 μm, which represents the experimental localization accuracy for this direction.

Subtracting the intrinsic dispersions of the localization method, which account for about 150 μm (as indicated in Section 4.4), and the known source width (150 μm), it is apparent that the residual value of about 400 μm r.m.s. represents the physical dispersion connected with the detection of a single photoelectron in the structure and is most likely due to the statistical fluctuation of the average position of the charge in the first amplification element. Indeed, it has been observed that a decrease in the avalanche size (obtained by increasing the TEA concentration) results in a better localization accuracy in the direction parallel to the anodes, but obviously the charge-interpolation probability decreases at the expense of the accuracy in the perpendicular direction (see below).

To understand better the interpolation process and the resulting localization properties, we have mounted the collimated photon source on a mechanical scanner with micrometer reading, and recorded the centre of gravity when displacing the

source by known amounts along the direction perpendicular to the anodes. A typical distribution measured for two positions of the collimator 1 mm away from each side of a wire are shown in Fig. 30; they have a width of 500 μm r.m.s. The results are summarized in Fig. 31, again for the argon-TEA 98.5-1.5 mixture; the correlation is obviously linear, showing the effectiveness of the interpolation mechanism, with an average dispersion of 500 μm. Subtracting again the source-width and electronics-dispersion contribution, the residual value of about 450 μm represents the intrinsic localization accuracy in the direction perpendicular to the anode wires, which is slightly worse than that for the parallel coordinate because of the fluctuation in the charge-sharing process.

We have repeated the same measurements in mixtures of helium and TEA, where the avalanche size appears to be smaller than for identical concentrations of TEA in argon. The effect of the reduction of the charge-interpolating events is visible in Fig. 32a, which is obtained using the same geometry as for Fig. 30; about 50% of all avalanches are detected by a single anode wire, and the discrete anode-wire structure appears clearly in the distribution. From the quoted charge-sharing ratio, and from Fig. 28, one infers an avalanche width of about 400 μm r.m.s. for these conditions; a direct measurement of the avalanche size in helium-TEA has, however, not been performed. Projection of the distribution in the direction parallel to the anodes, Fig. 32b, provides a value of about 350 μm r.m.s. for the accuracy along this coordinate. As expected, the physical dispersions on the avalanche centre of gravity are smaller for the smaller avalanche; subtracting as before the intrinsic resolution and the source-collimator width, we infer a residual fluctuation of about 280 μm (as compared to the 400 μm previously quoted).

A mechanical scanning along the direction perpendicular to the anode wires produces the results illustrated in Fig. 33. In this case, we have separately plotted the centre of gravity for events interesting a single anode wire (crosses) and charge-sharing events (squares). While for the second class a more or less linear correlation is observed, the single events obviously cluster around a position corresponding to the anode wire. A small right-left dependence is observed,

although of course the dispersions in the position determination prevent the identification of individual events.

The fact that, depending on the avalanche fluctuations, an event in a given position may or may not result in charge-sharing obviously increases the overall localization error for the coordinate perpendicular to the anode wires. It can be seen from Fig. 33 that this error varies between about 300 μm r.m.s. for a source position facing the wire up to about 600 μm at the edges.

Based on the quoted results it would seem convenient, in order to improve the localization accuracy when using a given number of readout channels, to increase the anode wire density, for example by a factor of two, grouping two adjacent wires on the same pulse-height measuring channel, and operating at a smaller avalanche size so as to reduce the dispersions in its centre of gravity still taking advantage of the charge-interpolation process.

REFERENCES

[1] J. Seguinot and T. Ypsilantis, Nucl. Instrum. Methods 142 (1977) 377.

[2] G. Coutrakon, J.R. Hubbard, Ph. Mangeot, G. Charpak, A. Peisert, F. Sauli, H. Glass, I. Kirz and R.L. McCarthy, Progress in Cherenkov ring imaging, Part 2: Identification of particles at 200 GeV/c (To be submitted to Nucl. Instrum. Methods, 1982).

[3] S.C. Curran and J.D. Craggs, Counting tubes (Butterworth, London 1941).

[4] H.S. Snyder, Phys. Rev. 72 (1947) 181.

[5] H. Schlumbohm, Z. Phys. 151 (1958) 563.

[6] T. Byrne, Proc. Soc. Edinburgh Sect. A 66 (1962) 33.

[7] A. Lansiart and P. Morucci, J. Phys. Radium 23, Suppl. 6 (1966) 102A.

[8] W. Legler, Brit. J. Appl. Phys. 18 (1967) 1275.

[9] G.D. Alkhazov, Nucl. Instrum. Methods 89 (1970) 155.

[10] F. Sauli, Principles of operation of multiwire proportional and drift chambers, CERN 77-09 (1977).

[11] E. Barrelet, T. Ekelöf, B. Lund-Jensen, J. Séguinot, J. Tocqueville, M. Urban and T. Ypsilantis, Submitted to Nucl. Instrum. Methods (Jan. 1982).

[12] G. Charpak and F. Sauli, Phys. Lett. 78B (1978) 523.

[13] G. Charpak, S. Majewski, G. Melchart, F. Sauli and T. Ypsilantis, Nucl. Instrum. Methods 164 (1979) 419.

[14] A. Breskin, G. Charpak, S. Majewski, G. Melchart, A. Peisert, F. Sauli, F. Mathy and G. Petersen, Nucl. Instrum. Methods 178 (1980) 11.

[15] J.R. Hubbard, G. Coutrakon, M. Cribier, Ph. Mangeot, H. Martin, J. Mullie, S. Palanque and J. Pelle, Nucl. Instrum. Methods 176 (1980) 293.

[16] G. Charpak, A. Peisert, F. Sauli, A. Cavestro, M. Vascon and G. Zanella, Nucl. Instrum. Methods 180 (1981) 387.

[17] A. Cattai, Thesis, presented at the University of Trieste, Italy (July 1981).

[18] M. Suzuki and S. Kubota, Nucl. Instrum. Methods 164 (1979) 197.

[19] J. Séguinot, J. Tocqueville and T. Ypsilantis, Nucl. Instrum. Methods 173, (1980) 283.

[20] G. Charpak and F. Sauli, Nucl. Instrum. Methods 113 (1973) 381.

Table 1

Construction parameters of the detector

| Electrode | Type | Pitch (mm) | Diameter (μm) | Gap (mm) |
|---|---|---|---|---|
| 1 | Mesh | 0.5 | 50 | 6 |
| 2 | Mesh | 0.5 | 50 | 4 |
| 3 | Mesh | 0.5 | 50 | 10 |
| 4 | Wires | 1.27 | 50 | 5 |
| 5 | Wires | 2.0 | 20 | 5 |
| 6 | Wires | 1.27 | 50 | |

Figure captions

Fig. 1 : Avalanche-size distributions for single electrons multiplying in methylal at increasing values of the reduced field [(a) to (e)]; to keep the average size roughly constant, the gap width has been reduced correspondingly. The transition from exponential to peaked distribution is evident . (From Ref. 5.)

Fig. 2 : Transition from proportional (top trace) to Geiger regime (lower trace) observed in a multiwire proportional chamber operated with 2% TEA in helium, at gains around $10^5$.

Fig. 3 : Secondary avalanches generated by electron photoproduction on the cathodes. The chamber was operated with 1‰ TMAE in argon at gains slightly in excess of $10^4$.

Fig. 4 : Schematics of the multistep proportional chamber. Charges produced by an ionizing event in the conversion region drift into the high-field preamplification space where an avalanche grows. A fraction of the electrons in the avalanche head proceed into the transfer region and receive further amplification in the multiwire proportional chamber.

Fig. 5 : Measured transverse distribution of electron charge in an avalanche developing in a 4 mm thick gap at gains around $10^4$, in a gas mixture containing 0.5% TEA in argon [17].

Fig. 6 : Transverse avalanche size in a 4 mm gap, at gains around $10^4$, measured as a function of TEA concentration in argon. A constant source-width contribution, estimated to be about 200 μm r.m.s. has not been subtracted from the data [17].

Fig. 7 : Efficiency of charge transfer from the preamplification into the transfer region, computed for several avalanche sizes (their standard deviation is indicated on the plots, in millimetres). The ordinate represents the distance of the avalanche centre from the boundary between two wires in the transfer mesh, with 0.5 mm pitch. For an avalanche size exceeding 200 μm r.m.s., the transfer efficiency tends to be uniform and equal to the ratio of fields in the transfer and preamplification regions (20% in the example).

Fig. 8 : Pulse-height distribution in the detection of single electrons recorded with a multistep proportional chamber operated with 1.5% TEA in argon at increasing values of the overall gain. The ordinate is given in terms of the detected charge; 1 pC corresponds to a gain of about $6 \times 10^6$. The peaked structure at large gains is apparent.

Fig. 9 : Schematic cross-section of the multistep proportional chamber used for the tests. A stack of fibre-glass frames holds the various electrodes that constitute the structure; on one side of the stack is mounted the $CaF_2$ window, while on the other a double mylar foil guarantees the gas-tightness. The insets show two possible solutions to the edge-breakdown problems encountered in the preamplification gap: an insulating foil inset (a) and a gap reducer (b).

Fig. 10 : Multiplication factor measured in a 4 mm thick parallel field gap for 1.5% TEA in helium.

Fig. 11 : Three possible ways of mounting $CaF_2$ crystals on thin frames, in order to implement large-surface composite windows. The scheme shown in (a) which uses thin compression bars and O-rings, was found to be not sufficiently gas-tight. Glueing with soft silicon rubber (b) was mechanically acceptable but showed large permeability to TEA; the third scheme (c), which couples the rigid support to the crystals through a flexible frame, gave satisfactory results.

Fig. 12 : A four-crystal mount used for testing the photon detector; each crystal is 100 × 100 $mm^2$ and 4 mm thick.

Fig. 13 : The VUV photon source used for measuring efficiency and localization properties of the detector. 5 MeV $\alpha$ particles emitted by the $^{24}Am$ source stop in the gas between two electrodes producing both ion pairs and scintillation photons; using krypton as the filling, the photon emission is centred around 1450 Å at peak TEA quantum efficiency. The charge signal, detected on the top mesh, can be used for coincidence measurements; moreover, the photon emission can be largely increased by applying a suitable difference of potential.

Fig. 14 : Electronic circuit of the charge preamplifier and receiver for the cathode (positive) signals; the anodic circuit uses complementary transistors.

Fig. 15 : The multistep proportional photon detector used for the measurements; it has a 200 × 200 $mm^2$ active area, fully equipped with charge preamplifiers on each anode wire and on cathode wire strips. To help reconstruction, the two cathode planes are perpendicular to each other and the anode wires are mounted at 45° to the cathodes.

Fig. 16 : As part of the calibration procedure, we record the pulse-height distribution for $^{55}Fe$ 5.9 keV X-rays for all channels. The figure shows a typical spectrum obtained on an anode wire, operating the detector at low gain with argon-TEA. A similar distribution is obtained for the cathode strips, under the restrictive condition that the strip contained the computed centre of gravity of the induced cluster.

Fig. 17 : Scatter plot of the difference between the directly measured coordinate y and its value computed from the other pair of coordinates, as a function of y itself. The deviations from linearity of the plot and its width represent the precision of the centre of gravity calibration. The projected distribution has 250 μm r.m.s.

Fig. 18 : Simulated effect of a variation by 50% of the gain on one of the cathode amplifiers mounted on the strip centred around y = 56 mm.

Fig. 19 : Relative efficiency plateaux in the detection of VUV photons with the multistep proportional chamber, as a function of the anodic potential and for three values of the preamplification voltage. The gas mixture is 1.5% TEA in helium.

Fig. 20 : Relative efficiency plateaux in the detection of VUV photons, for a gas mixture containing 1.5% TEA and 5% methane in helium.

Fig. 21 : Relative detection efficiency as a function of the drift voltage. A slight increase towards the higher fields may be due to increasing collection efficiency for photoelectrons produced very close to the window.

Fig. 22 : Pulse-height spectrum for single photoelectrons recorded on the cathodes when operating the detectors with 1.5% TEA in helium. For this measurement, a set of 10-bit charge-to-digital converters was used.

Fig. 23 : Correlation between the overall charge detected in each cluster by the two cathode planes.

Fig. 24 : Correlation between the charge detected on the anode and on one cathode plane.

Fig. 25 : Projection of the relative amplitude difference between the charge detected in the two cathodes; it has a FWHM of about 5%. The correlation has been exploited to couple multihit events properly in the case of clusters overlapping or ambiguous geometrical reconstruction.

Fig. 26 : Normalized charge distribution around the computed centre of gravity of cathode clusters. The distribution is roughly Gaussian with 8 mm FWHM.

Fig. 27 : An example of a double-cluster event, as seen on one cathode, and the Gaussian fit to two distributions with a known standard deviation (as from Fig. 28).

Fig. 28 : Computed ratio of charge sharing versus total number of events for a multistep detector with 2 mm anode wire spacing, as a function of avalanche size in the preamplification gap.

Fig. 29 : Distribution of the computed centre of gravity in the detection of photons emitted from a source collimated in the direction perpendicular to the anode wires. In (a) the projection along the wires shows almost no structure owing to the large amount (80%) of charge-sharing events, in (b) the projection along the collimation direction provides the localization accuracy perpendicular to the anodes, which is 450 μm r.m.s. Gas filling: 1.5% TEA in argon.

Fig. 30 : Centre-of-gravity distribution for a source collimated in the direction parallel to the anode wires, for two positions 1 mm away from each side of the wire. The distributions have a width of about 500 μm r.m.s.

Fig. 31 : Average computed centre of gravity and dispersion as a function of the actual collimated source position, for the coordinate perpendicular to the anode wires. Owing to the fluctuations in the charge-sharing process the localization error, 500 μm r.m.s., is larger than for the other direction.

Fig. 32 : Distribution of the centre of gravity in the detection of photons for a source collimated in the direction perpendicular to the anodes, using 1.5% TEA in helium. The smaller avalanche size in this case implies a reduced number of charge-sharing events (around 50%). In (a) the peaked structure corresponding to the anode wire positions is obvious. Because of the smaller fluctuations in the avalanche shape, however, the localization accuracy in the direction parallel to the wires which is about 350 μm r.m.s. (b) is better than for the previous case.

Fig. 33 : Computed centre of gravity along the coordinate perpendicular to the anodes wires, as a function of the real source position. Open circles represent charge-sharing events, and follow a more or less linear relationship to the real position, while full points represent events where a single anode provided a significative charge and cluster around the actual wire position.

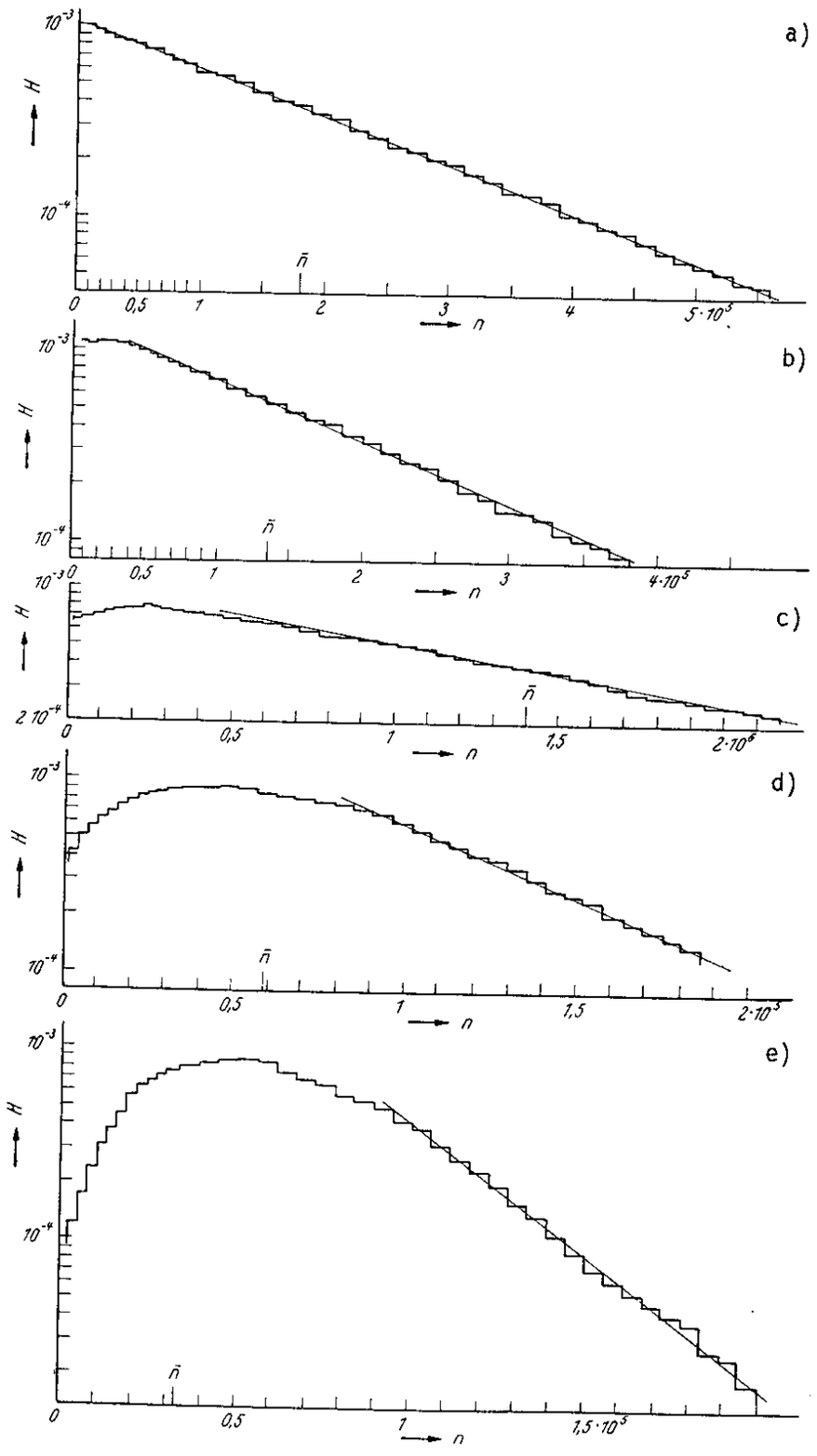
a)
b)
c)
d)
e)
H
n
$\bar{n}$
$10^{-3}$
$10^{-4}$
$2\,10^{-4}$
0
0,5
1
2
3
4
$5\cdot10^{5}$
$4\cdot10^{5}$
1,5
$2\cdot10^{5}$
$1,5\cdot10^{5}$

Fig. 1

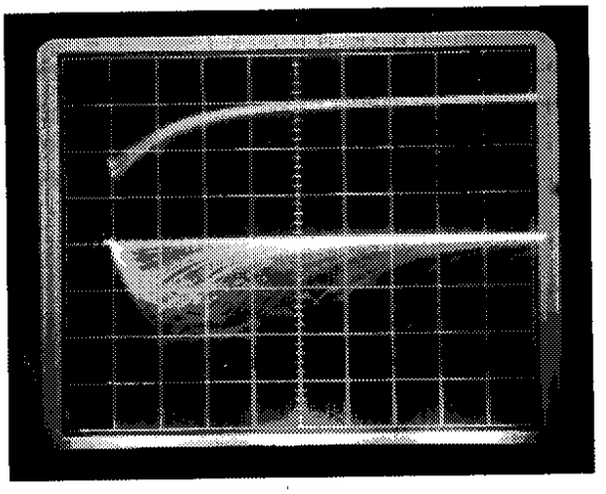

Fig. 2

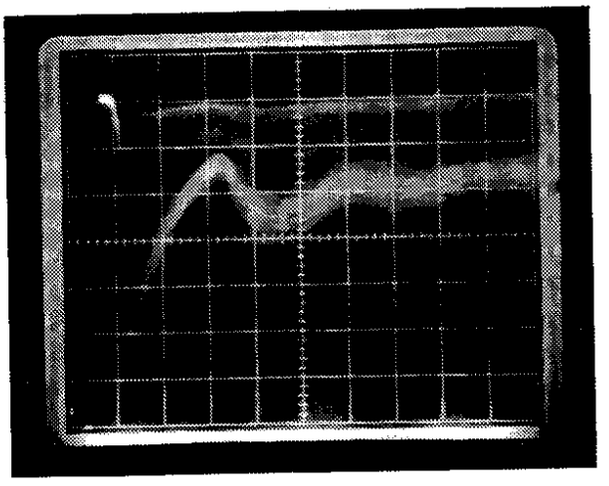

Fig. 3

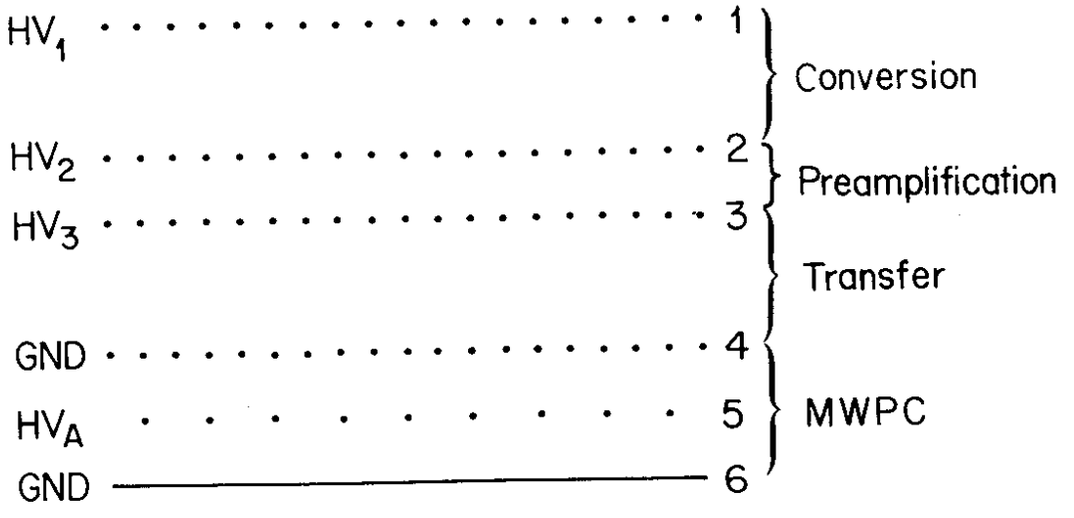


Fig. 4

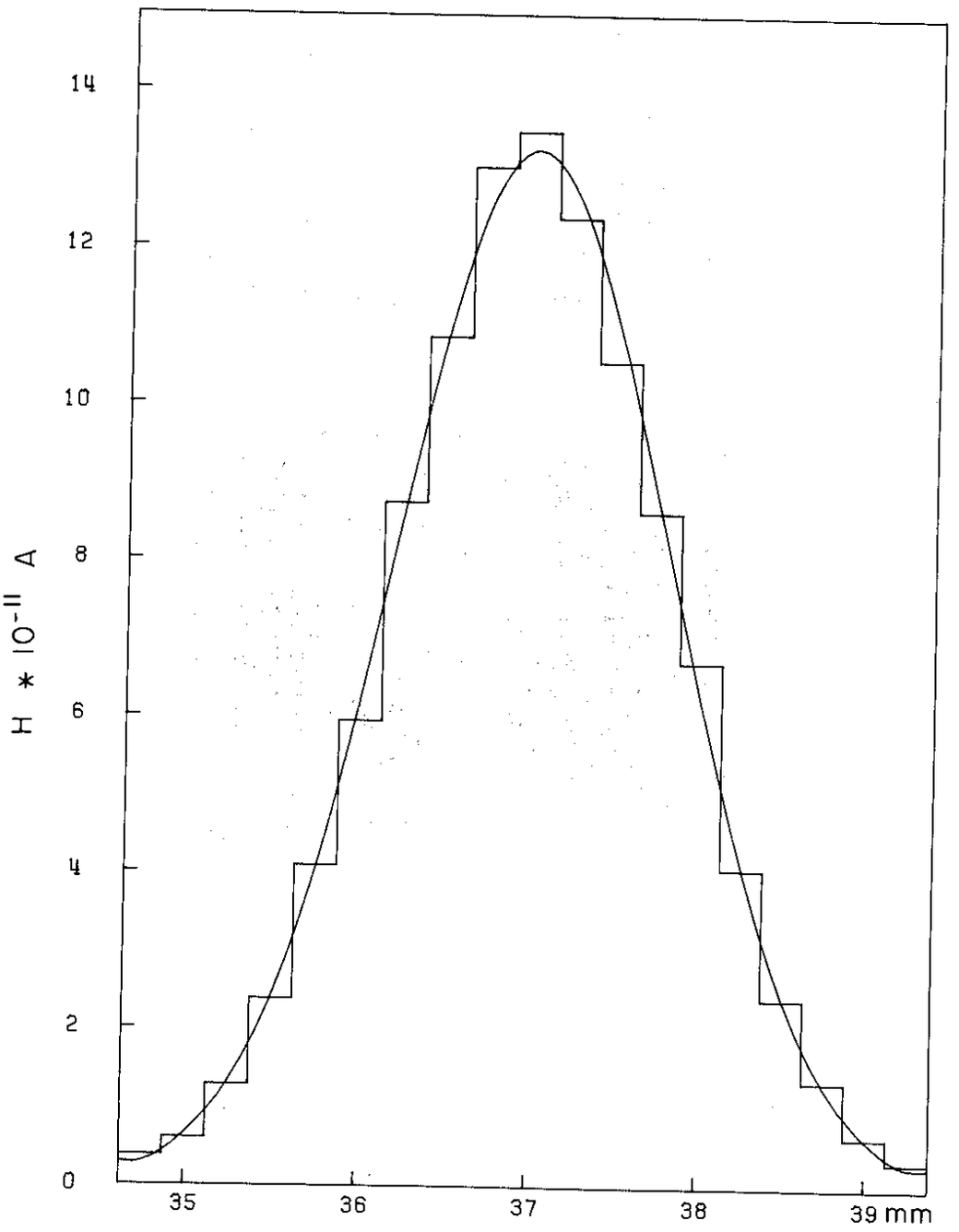


Fig. 5

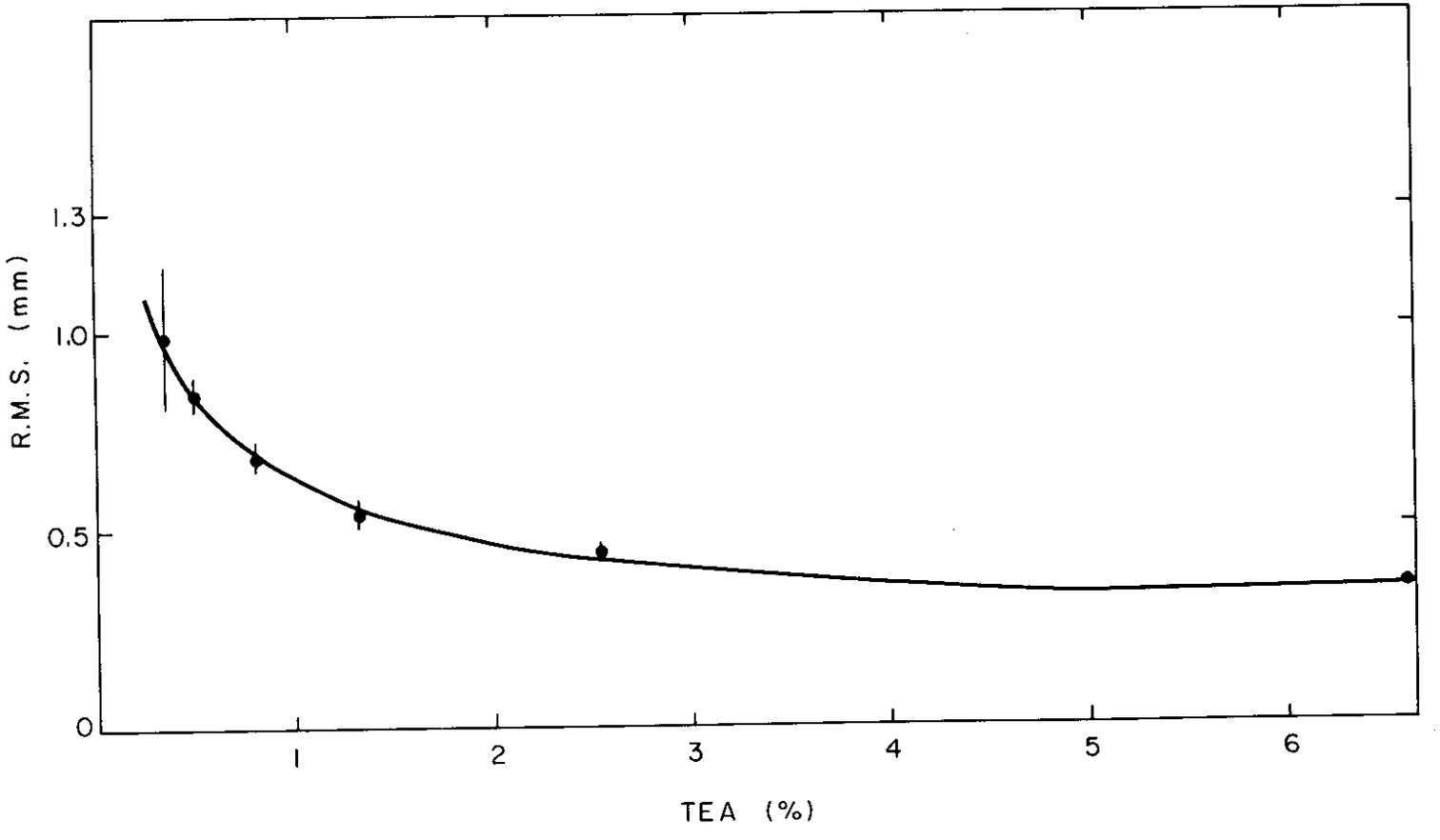


Fig. 6

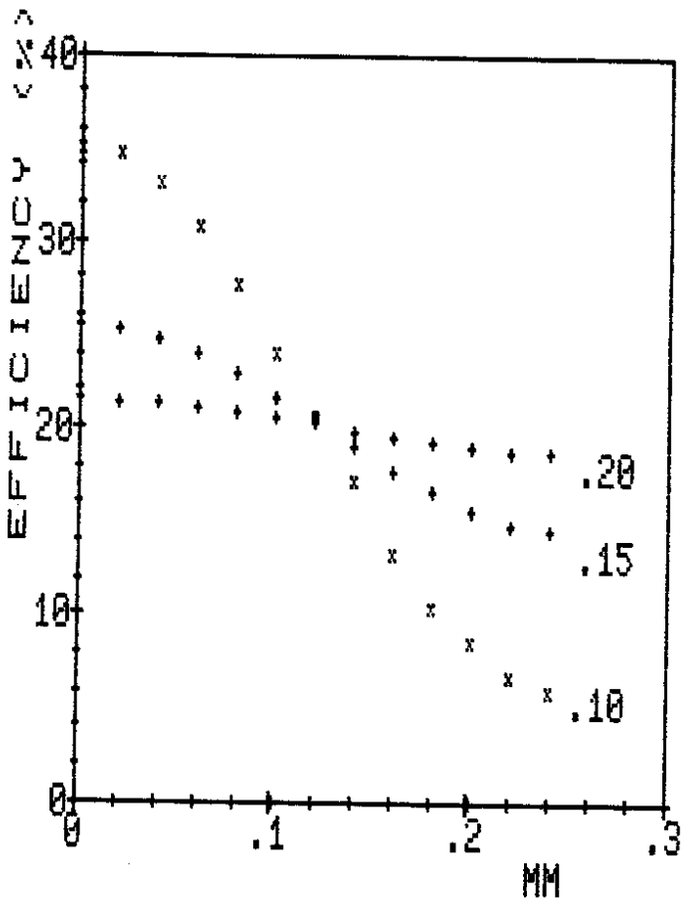
EFFICIENCY (%)
40
30
20
10
0
0
.1
.2
.3
MM
.20
.15
.10

Fig. 7

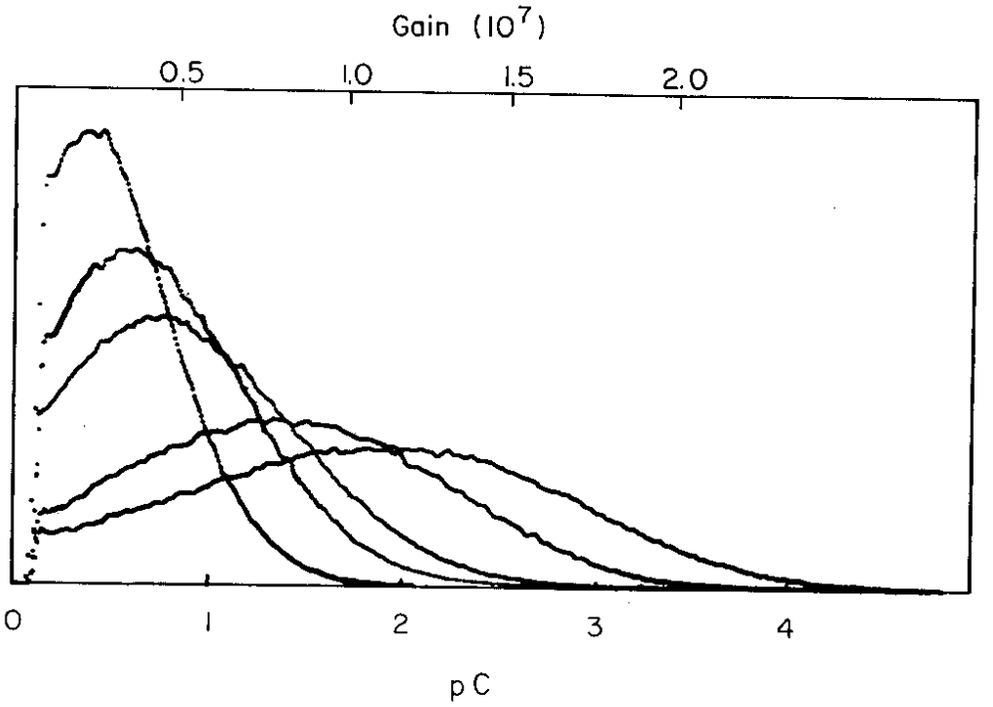
Gain ($10^7$)
0.5
1.0
1.5
2.0
0
1
2
3
4
pC

Fig. 8

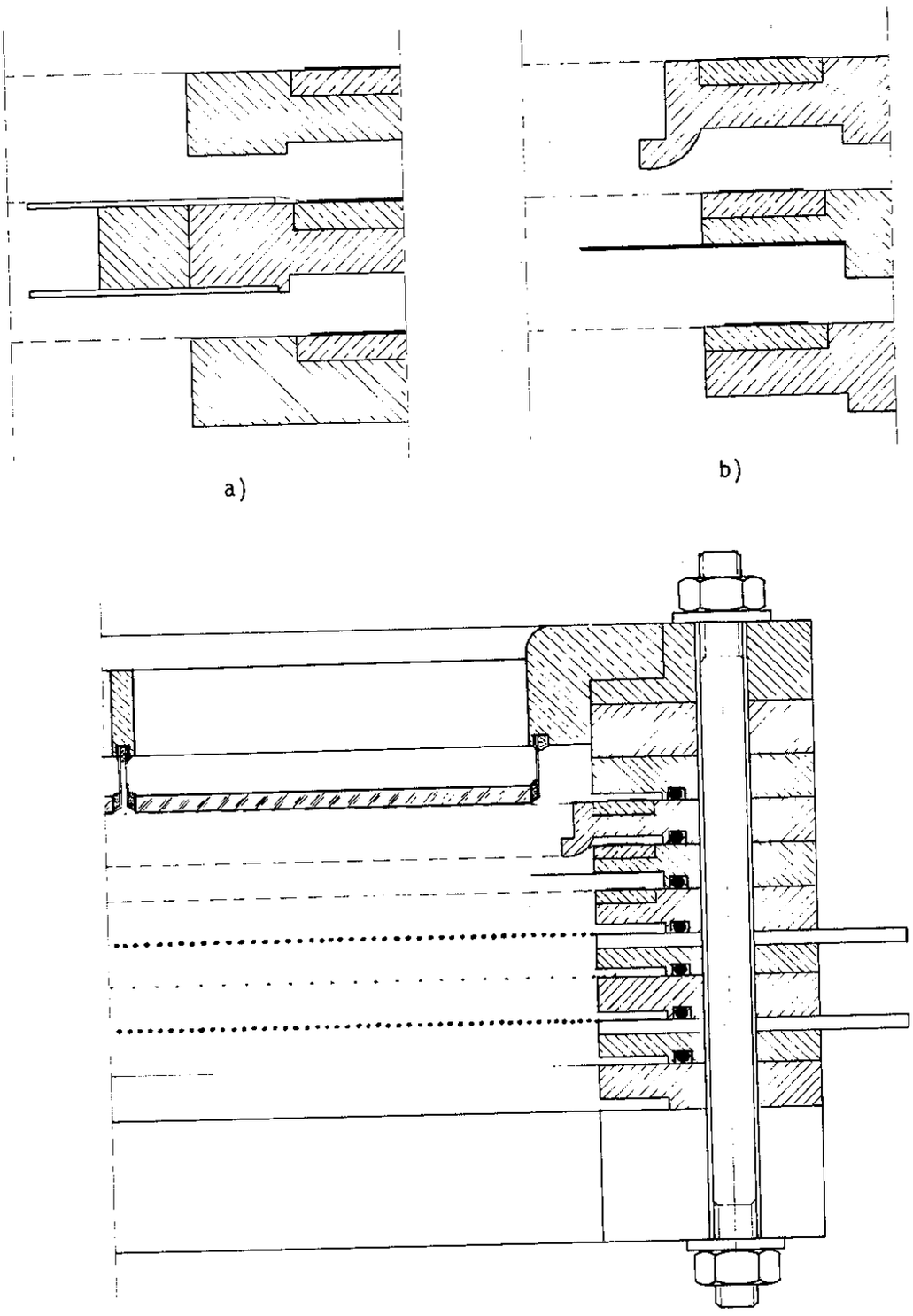


Fig. 9

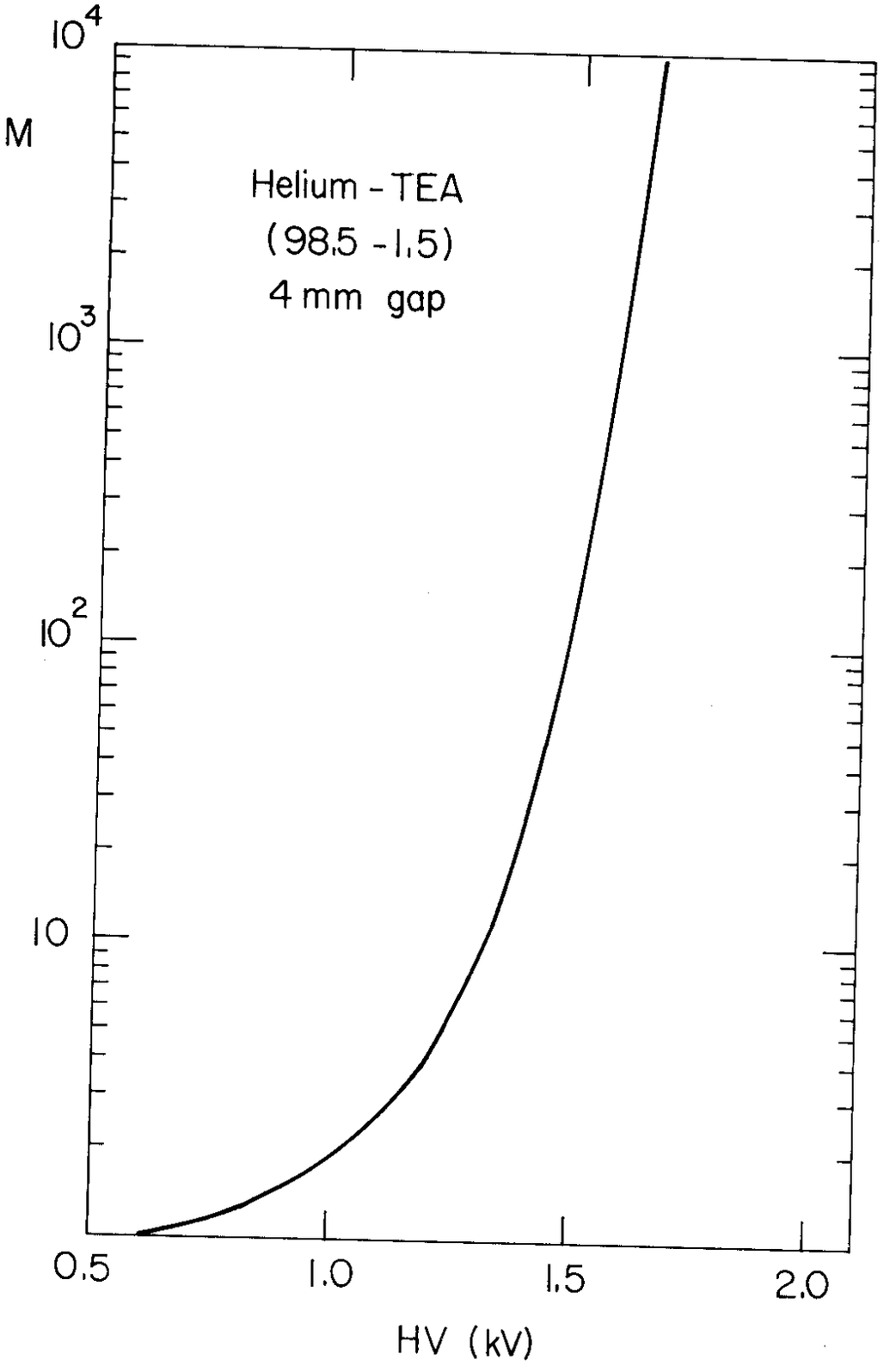


Fig. 10

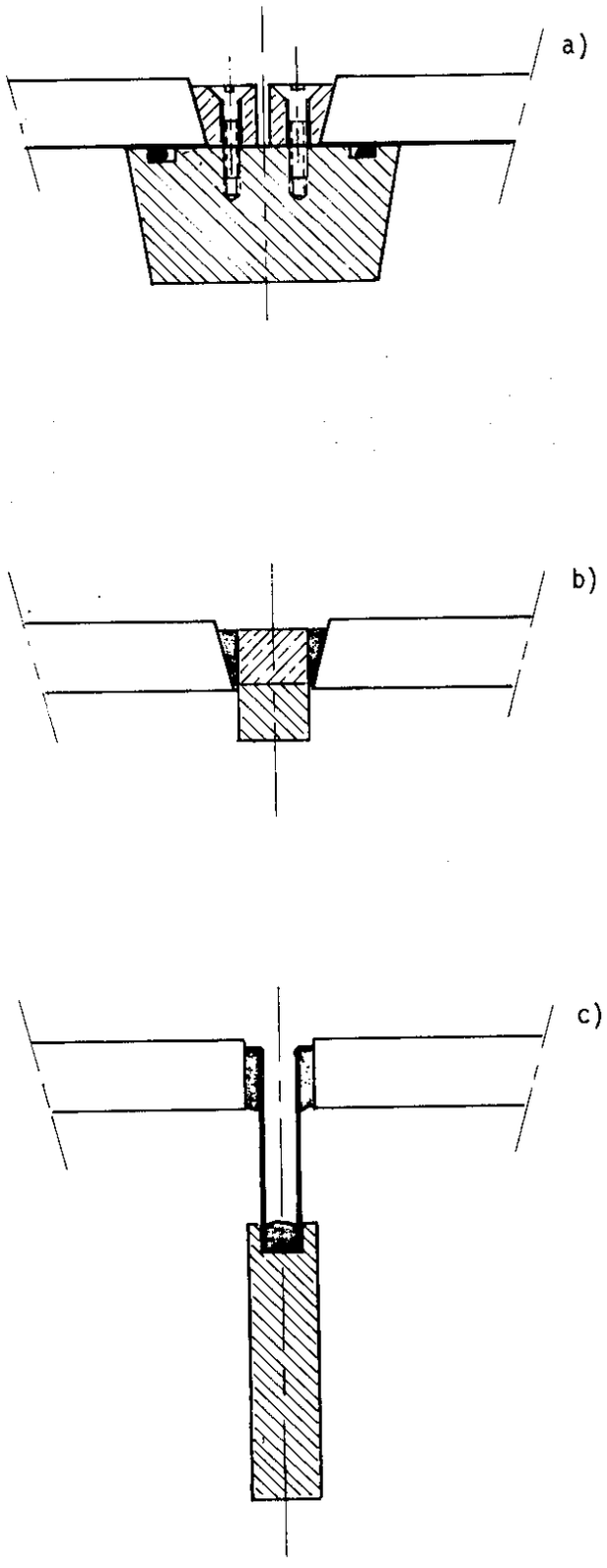


Fig. 11

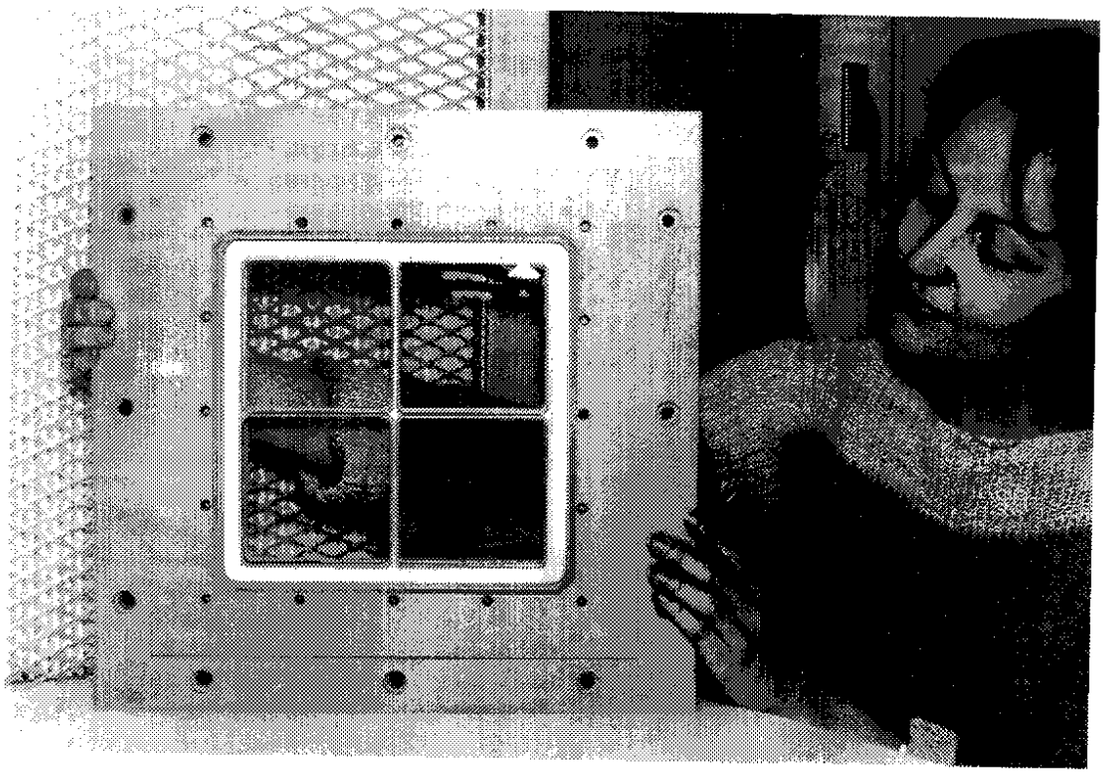

Fig. 12

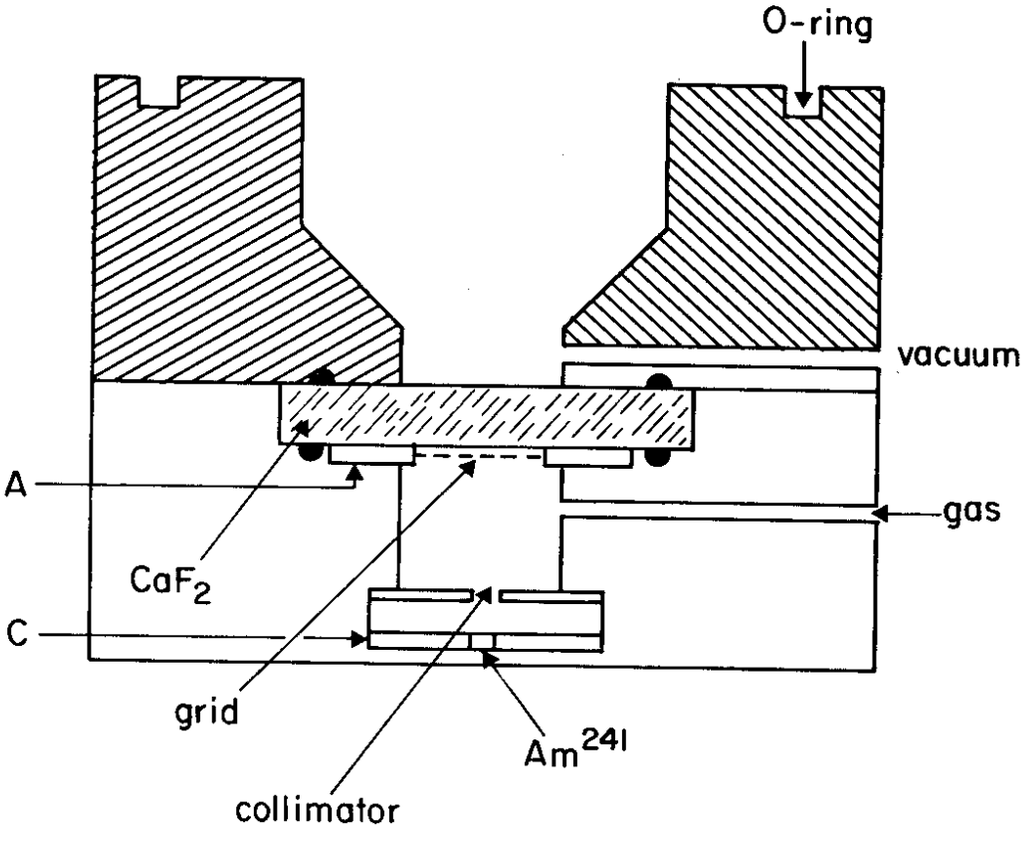


Fig. 13

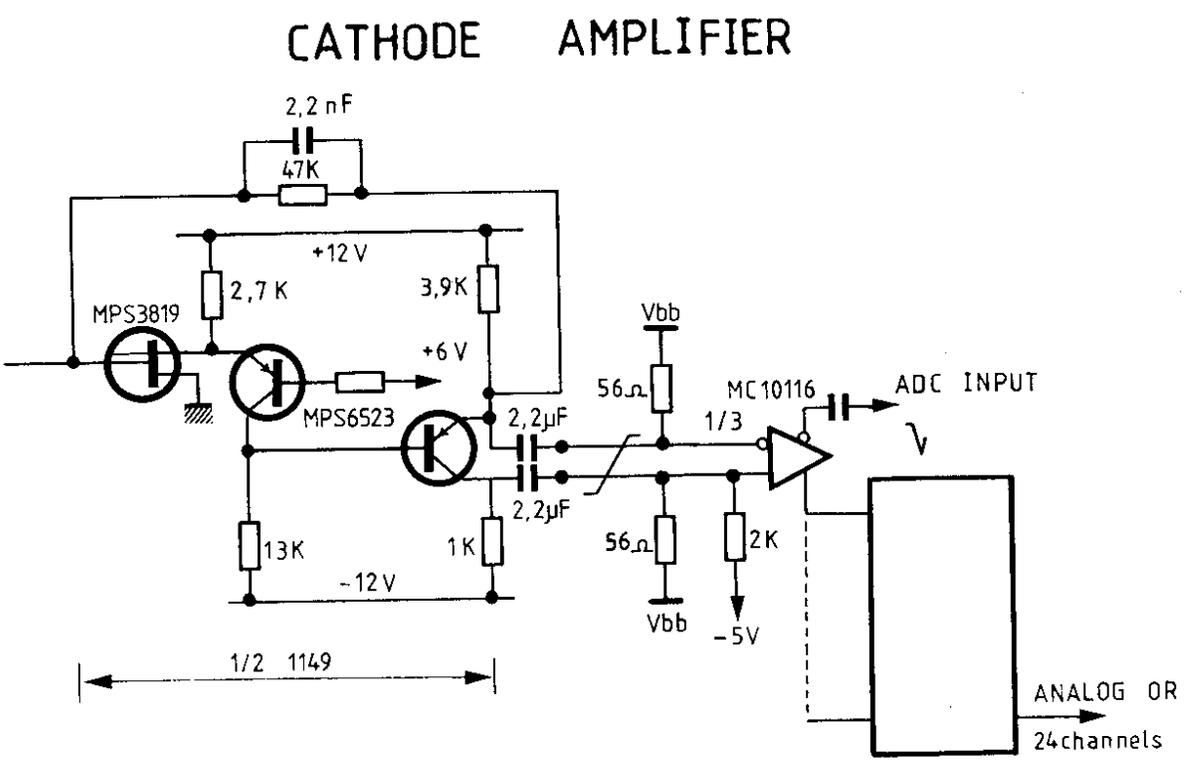
CATHODE AMPLIFIER
2,2 nF
47K
+12 V
2,7 K
3,9K
MPS3819
+6 V
MPS6523
Vbb
56Ω
MC10116
1/3
ADC INPUT
2,2µF
2,2µF
13K
1K
56Ω
2K
-12 V
Vbb
-5V
1/2 1149
ANALOG OR
24channels

Fig. 14

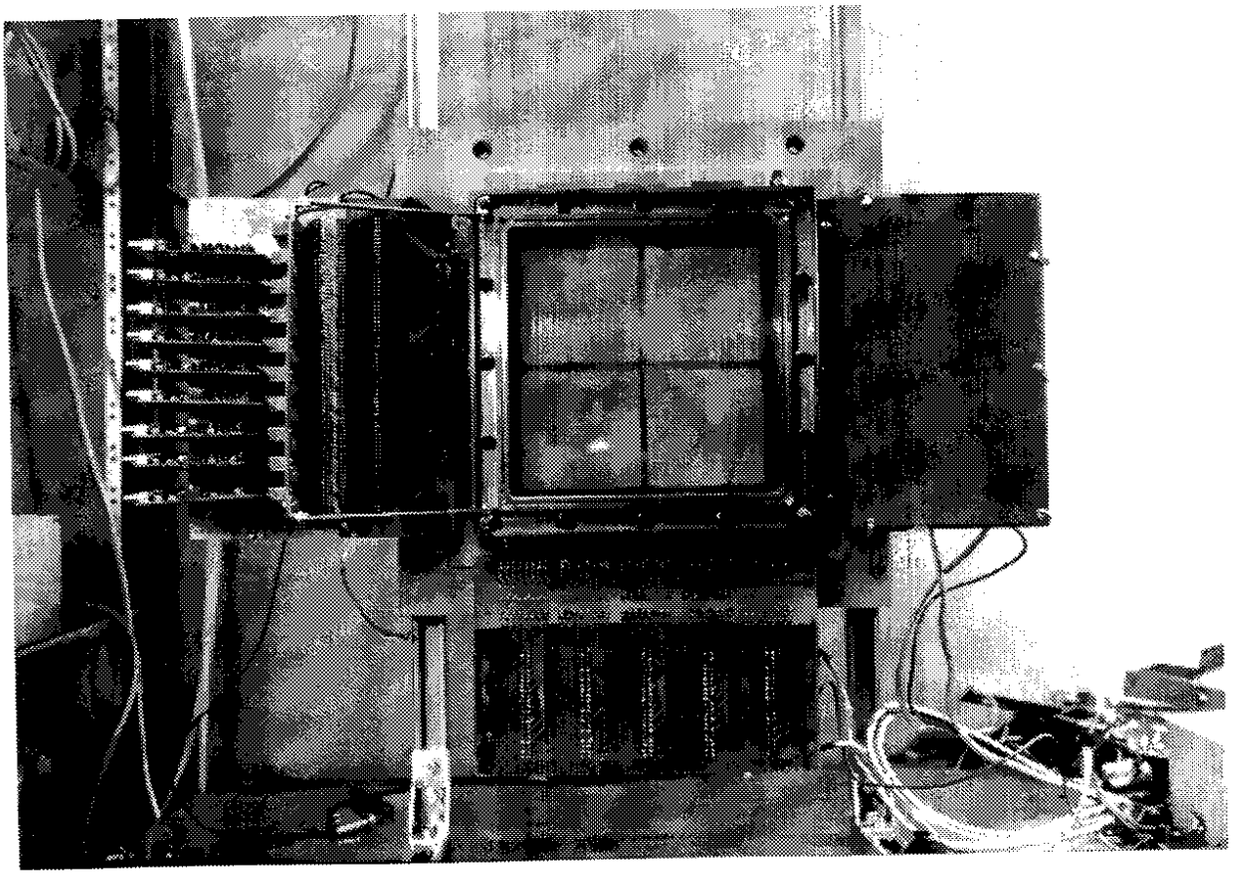

Fig. 15

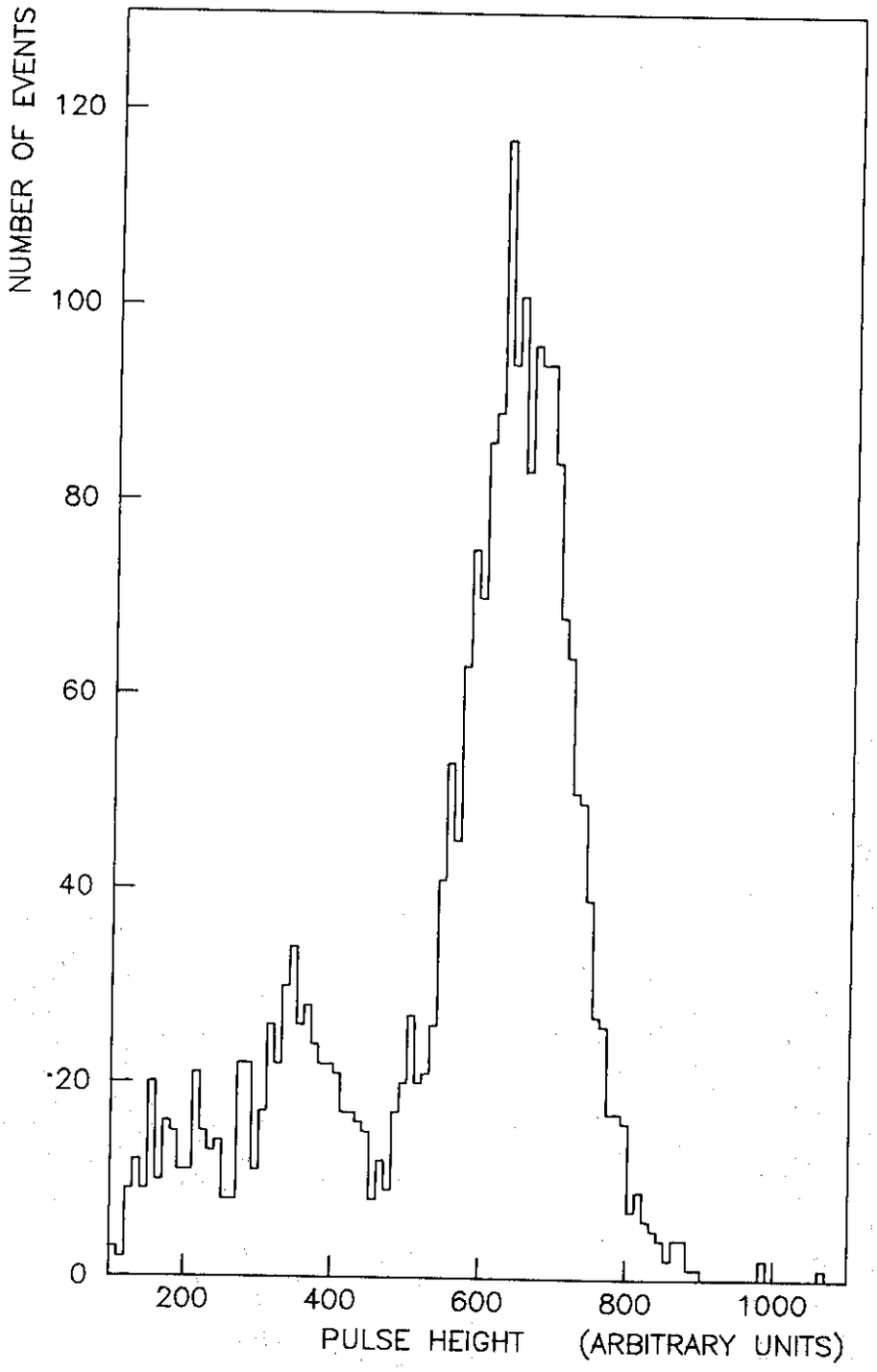
NUMBER OF EVENTS
120
100
80
60
40
20
0
200
400
600
800
1000
PULSE HEIGHT (ARBITRARY UNITS)

Fig. 16

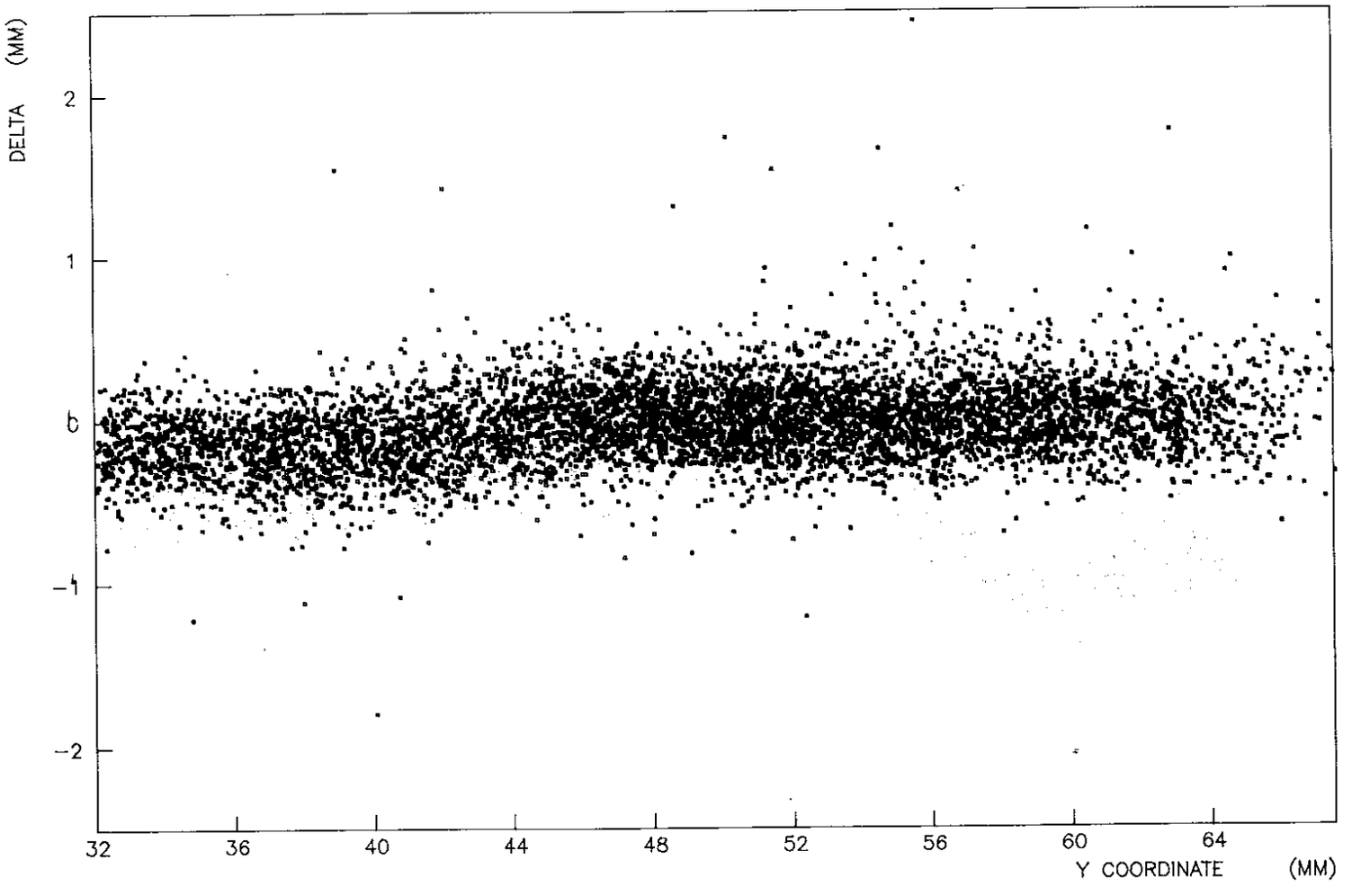


Fig. 17

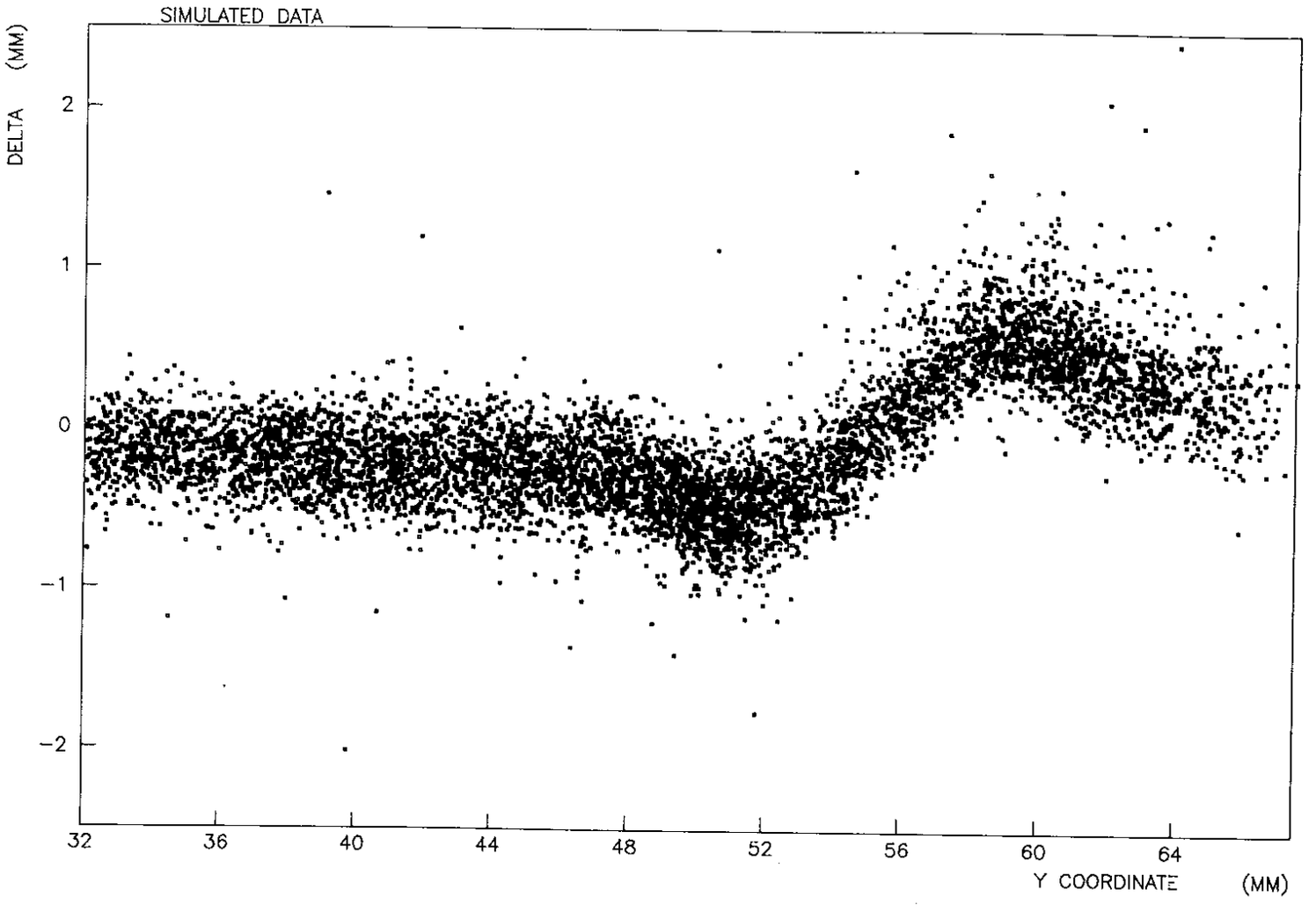
SIMULATED DATA
DELTA (MM)
2
1
0
−1
−2
32
36
40
44
48
52
56
60
64
Y COORDINATE (MM)

Fig. 18

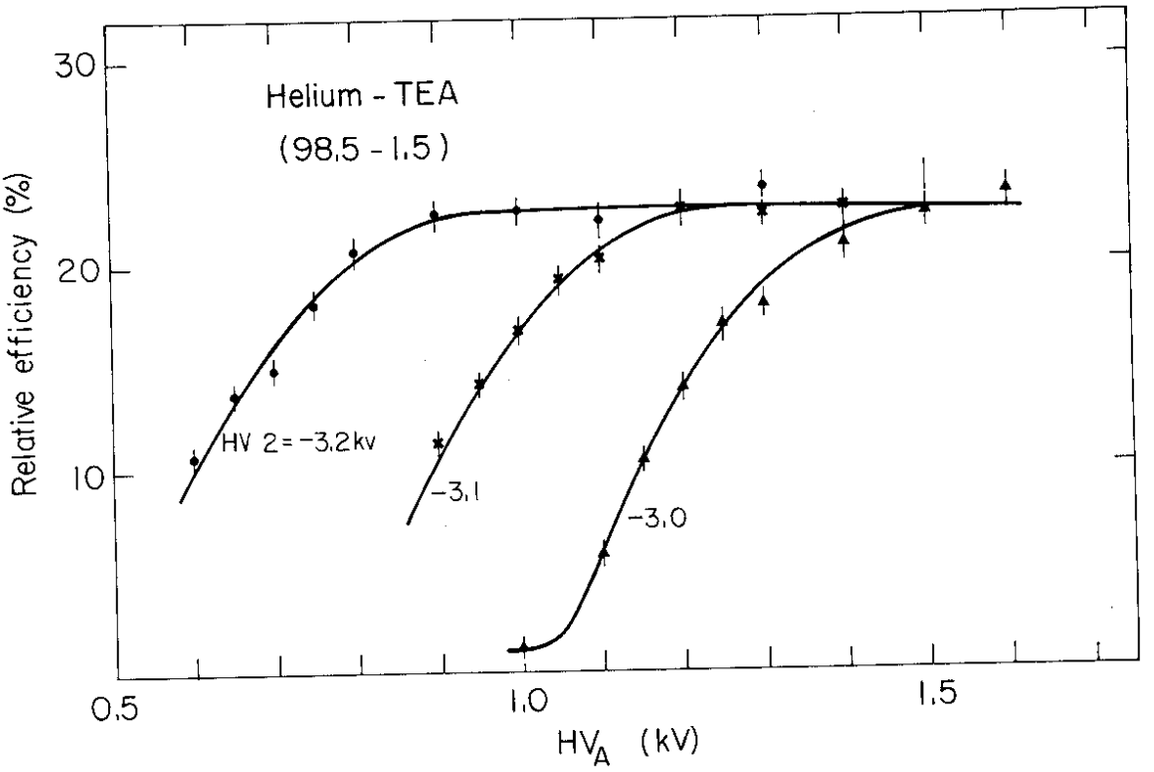
Helium - TEA
(98,5 - 1,5)
HV 2 = -3,2kv
-3,1
-3,0
Relative efficiency (%)
30
20
10
0,5
1,0
1,5
HV$_A$ (kV)

Fig. 19

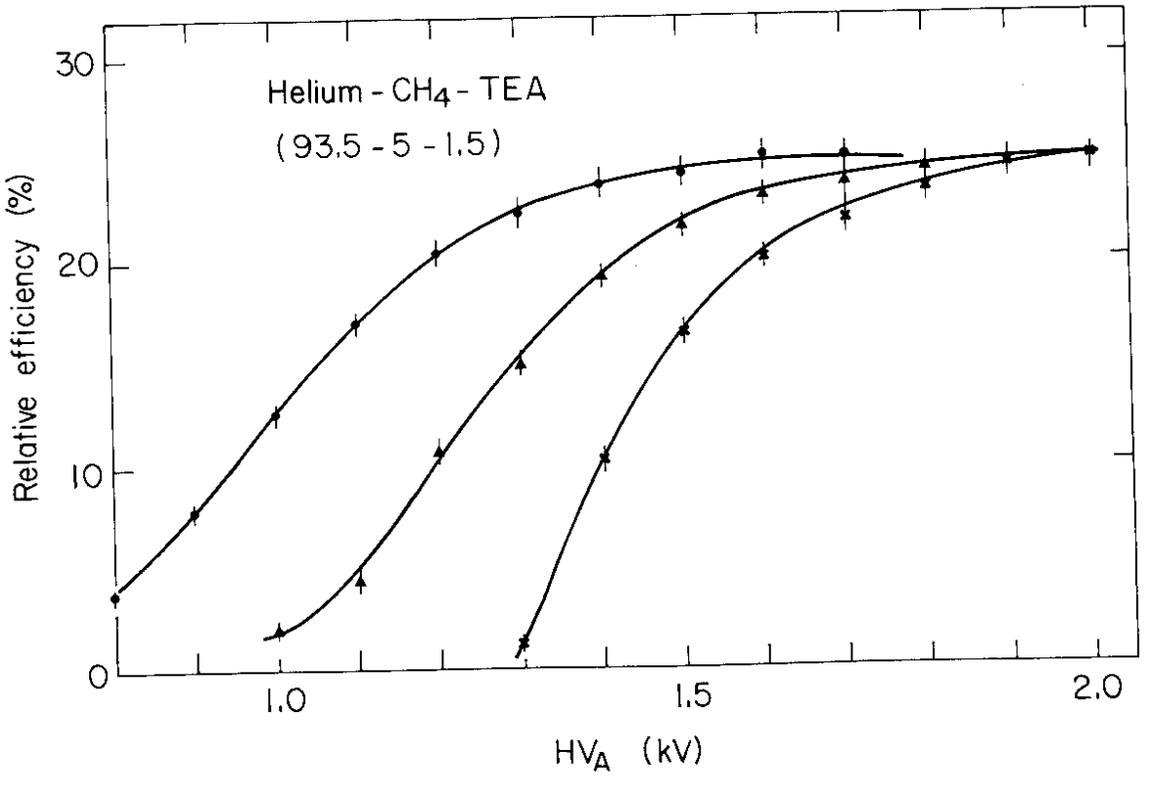
Helium - CH$_4$ - TEA
(93,5 - 5 - 1,5)
Relative efficiency (%)
30
20
10
0
1,0
1,5
2,0
HV$_A$ (kV)

Fig. 20

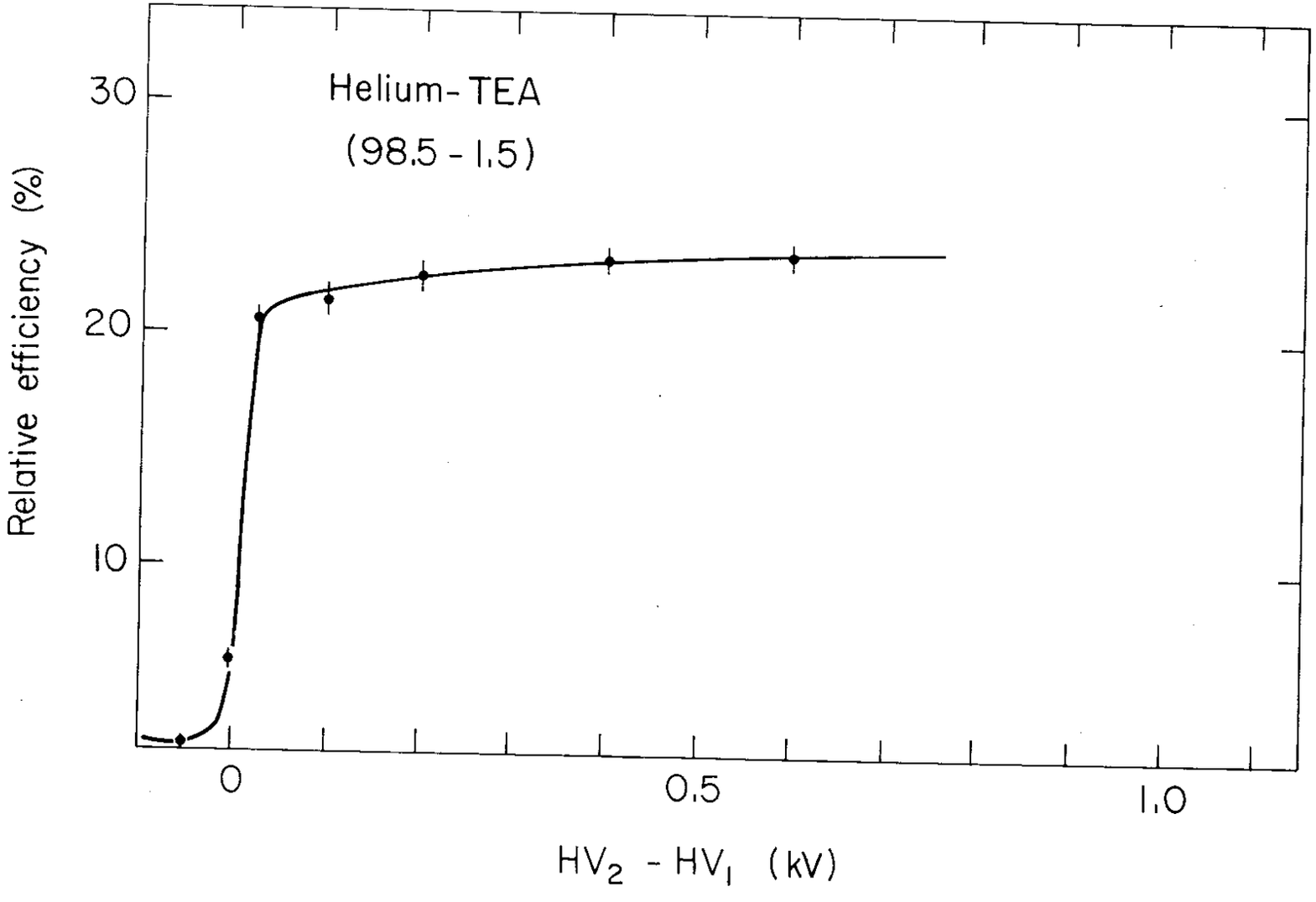
Helium-TEA
(98.5 - 1.5)
Relative efficiency (%)
30
20
10
0
0.5
1.0
HV2 - HV1 (kV)

Fig. 21

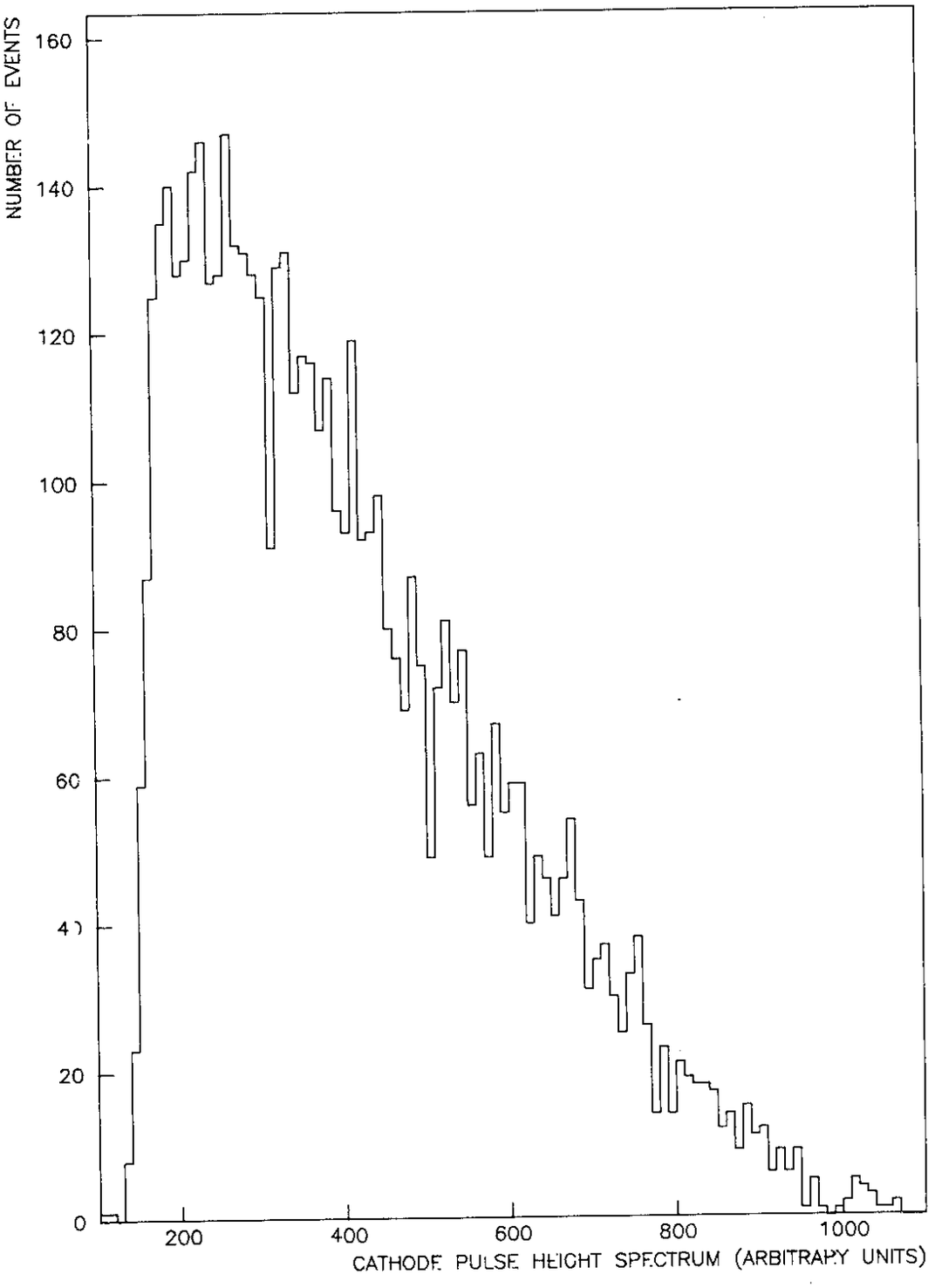
NUMBER OF EVENTS
160
140
120
100
80
60
40
20
0
200
400
600
800
1000
CATHODE PULSE HEIGHT SPECTRUM (ARBITRARY UNITS)

Fig. 22

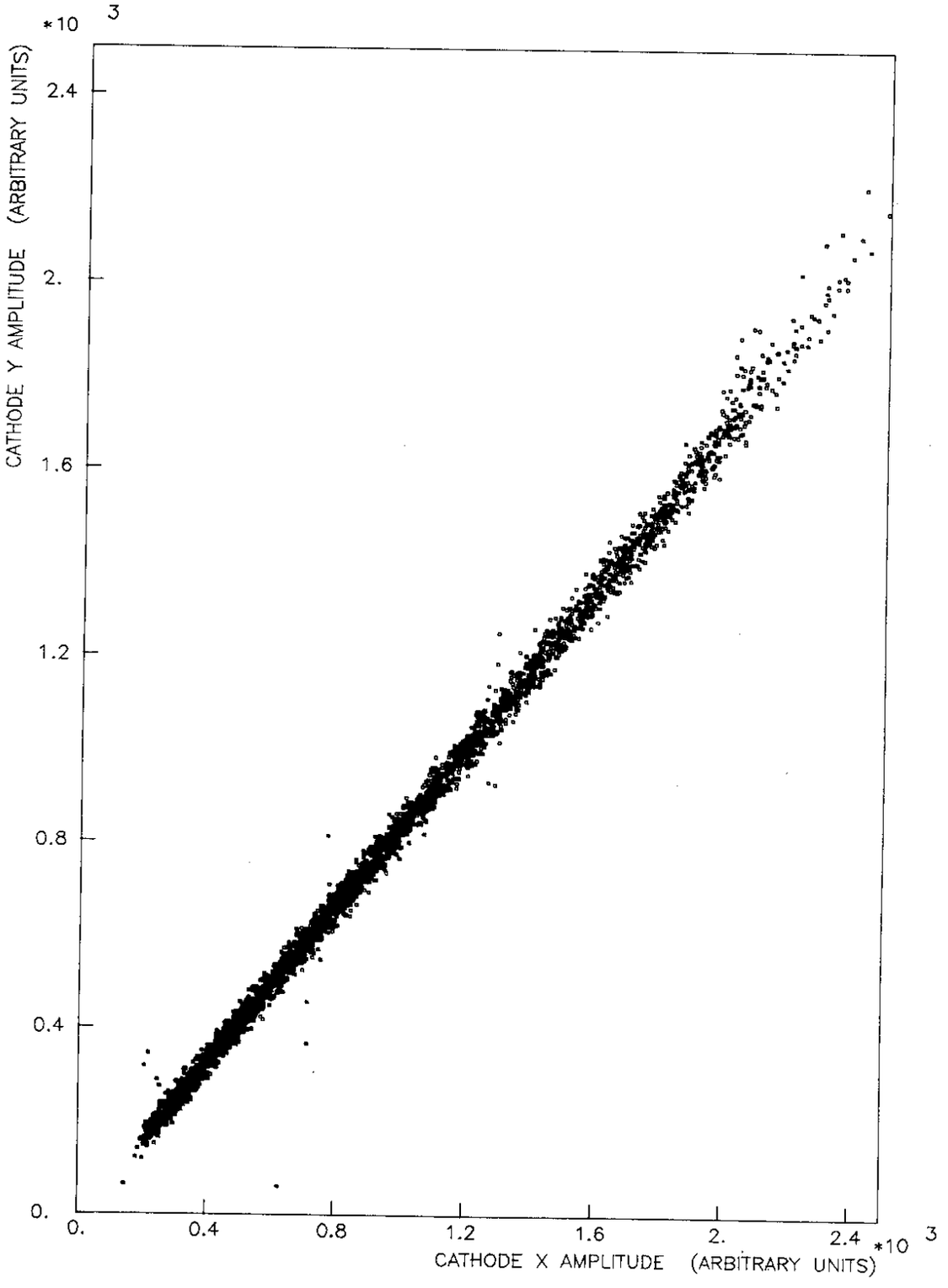
*10 3
2.4
2.
1.6
1.2
0.8
0.4
0.
CATHODE Y AMPLITUDE (ARBITRARY UNITS)
0.
0.4
0.8
1.2
1.6
2.
2.4 *10 3
CATHODE X AMPLITUDE (ARBITRARY UNITS)

Fig. 23

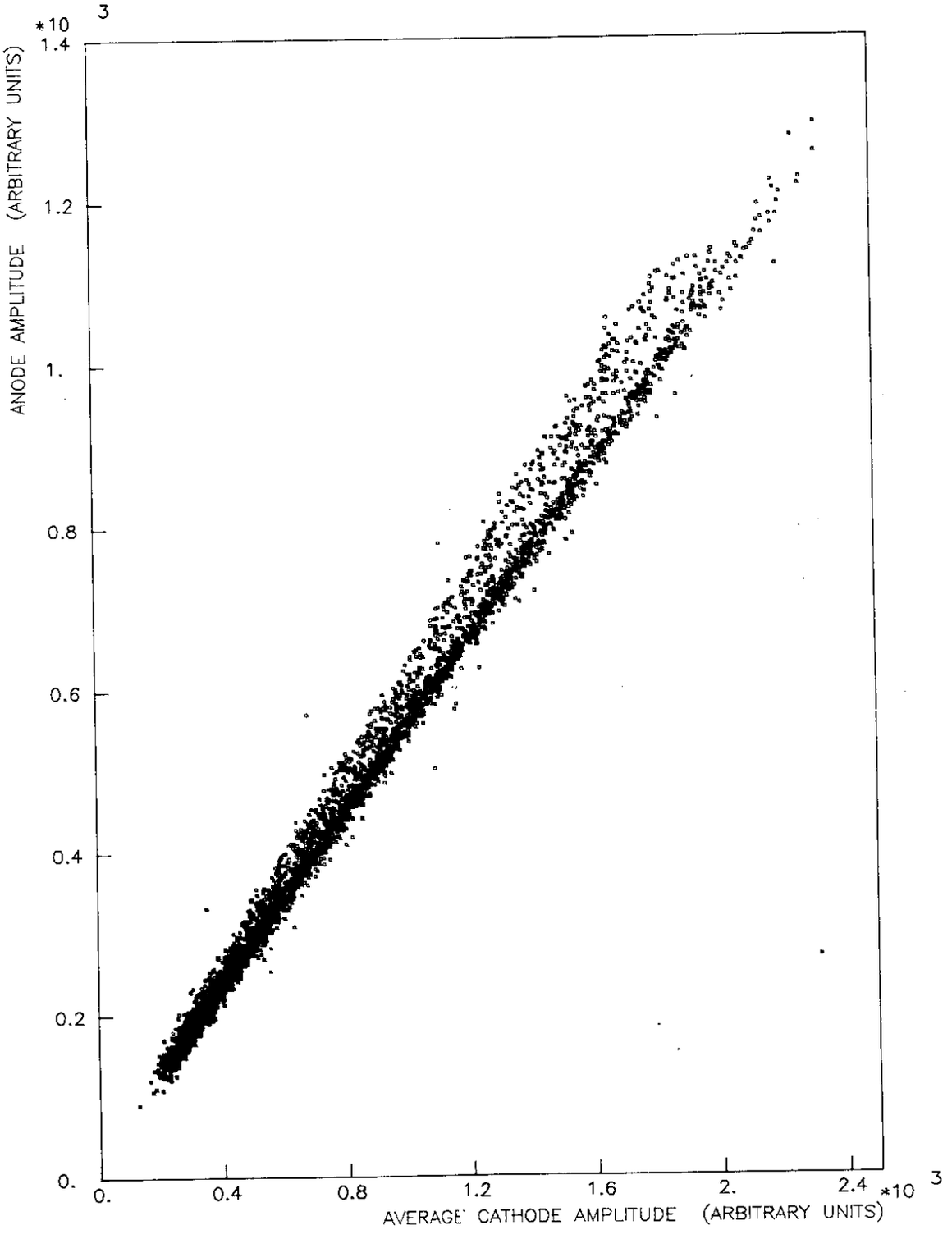
*10 3
1.4
1.2
1.
0.8
0.6
0.4
0.2
0.
ANODE AMPLITUDE (ARBITRARY UNITS)
0.
0.4
0.8
1.2
1.6
2.
2.4
*10 3
AVERAGE CATHODE AMPLITUDE (ARBITRARY UNITS)

Fig. 24

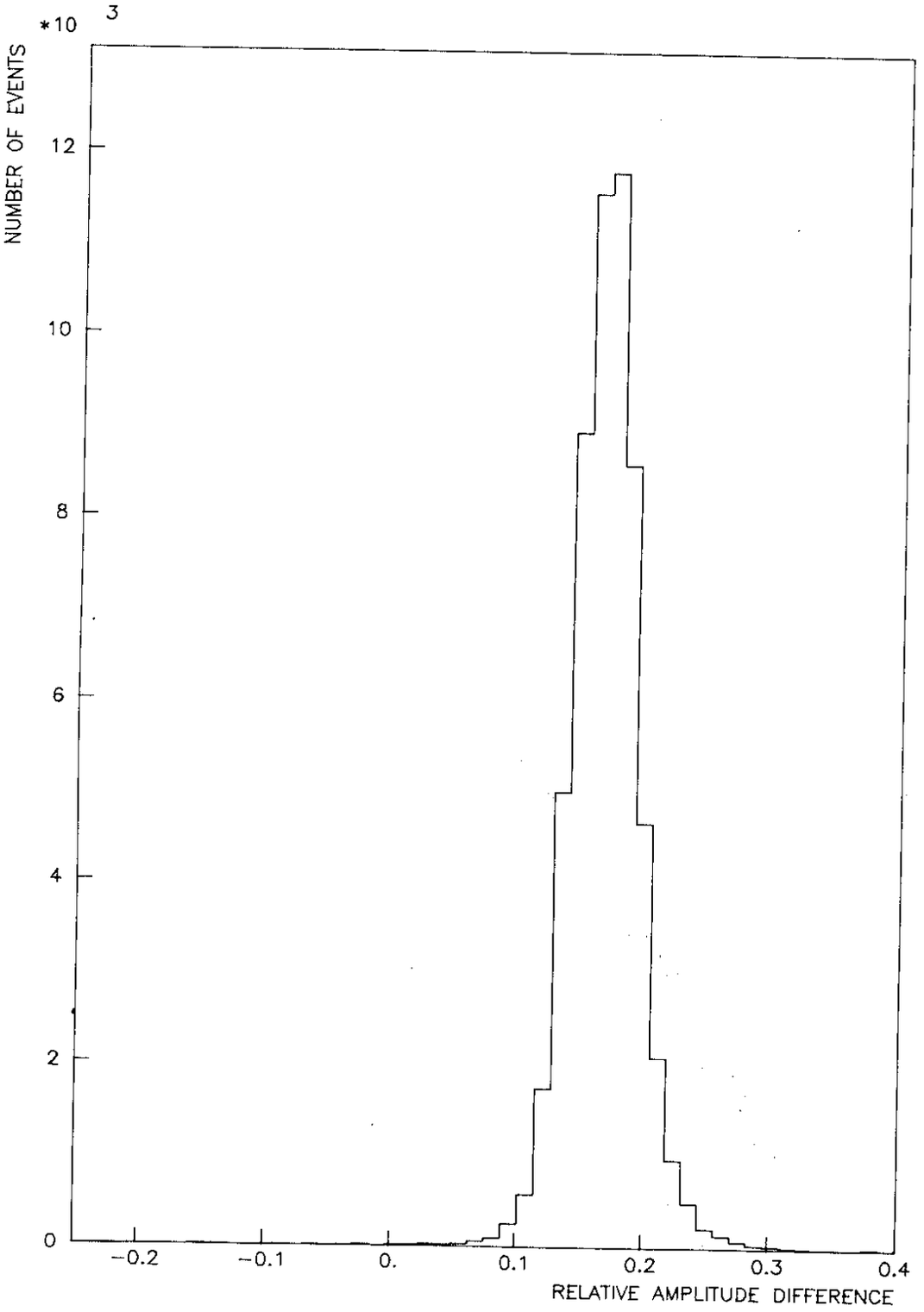
*10 3
NUMBER OF EVENTS
12
10
8
6
4
2
0
-0.2
-0.1
0.
0.1
0.2
0.3
0.4
RELATIVE AMPLITUDE DIFFERENCE

Fig. 25

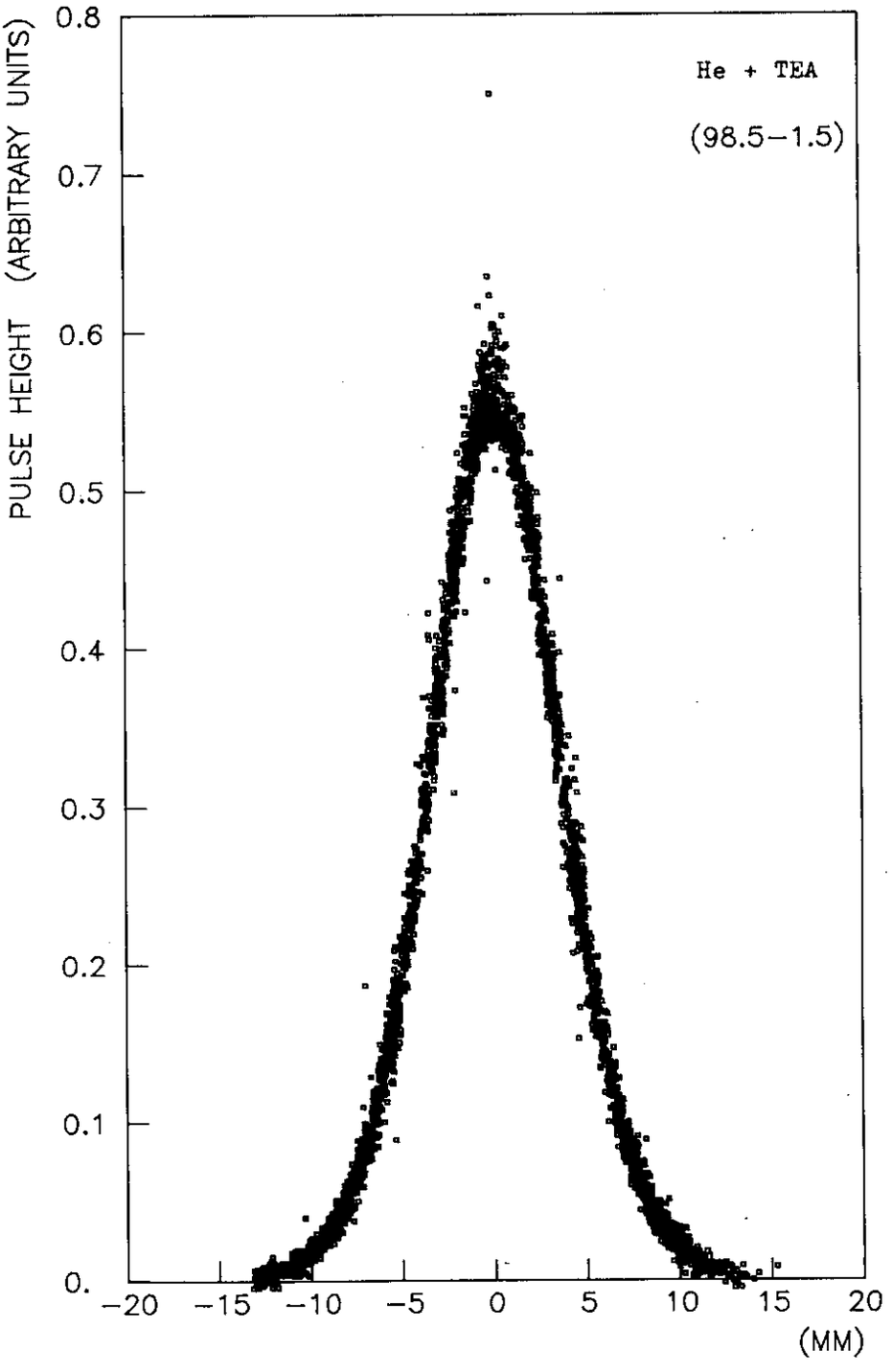
He + TEA
(98.5−1.5)
PULSE HEIGHT (ARBITRARY UNITS)
0.8
0.7
0.6
0.5
0.4
0.3
0.2
0.1
0.
−20
−15
−10
−5
0
5
10
15
20
(MM)

Fig. 26

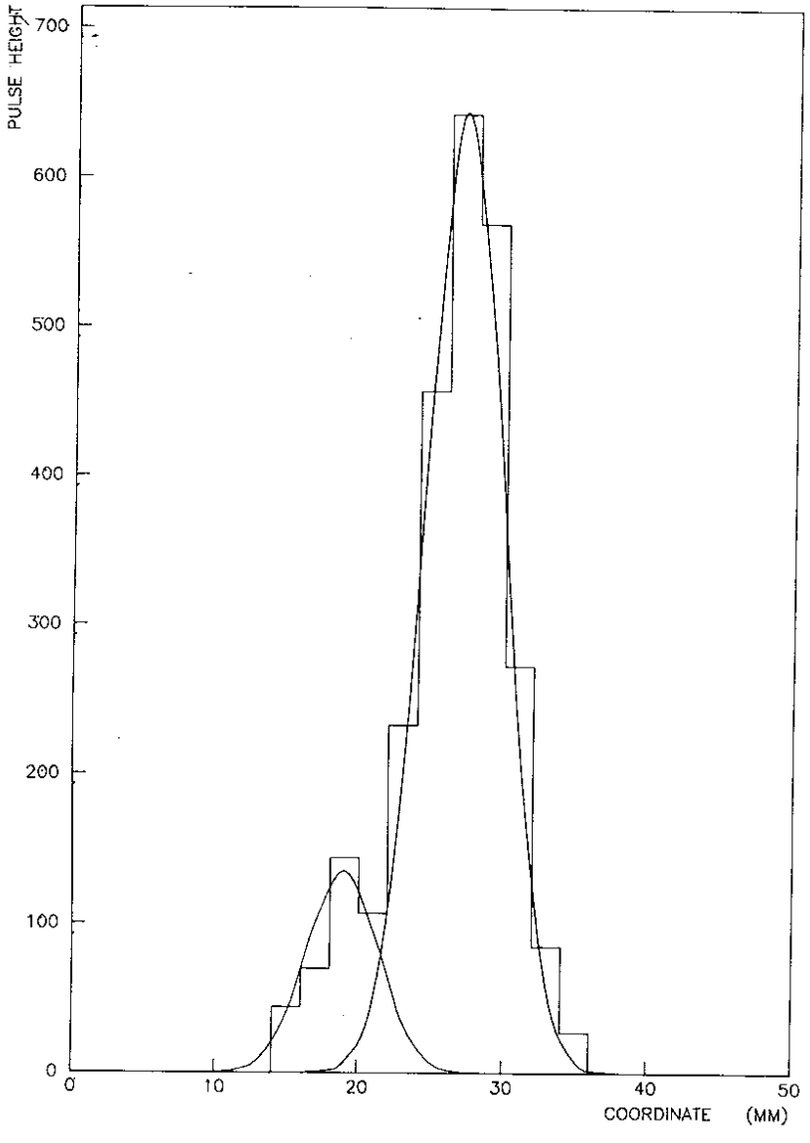
PULSE HEIGHT
700
600
500
400
300
200
100
0
0
10
20
30
40
50
COORDINATE (MM)

Fig. 27

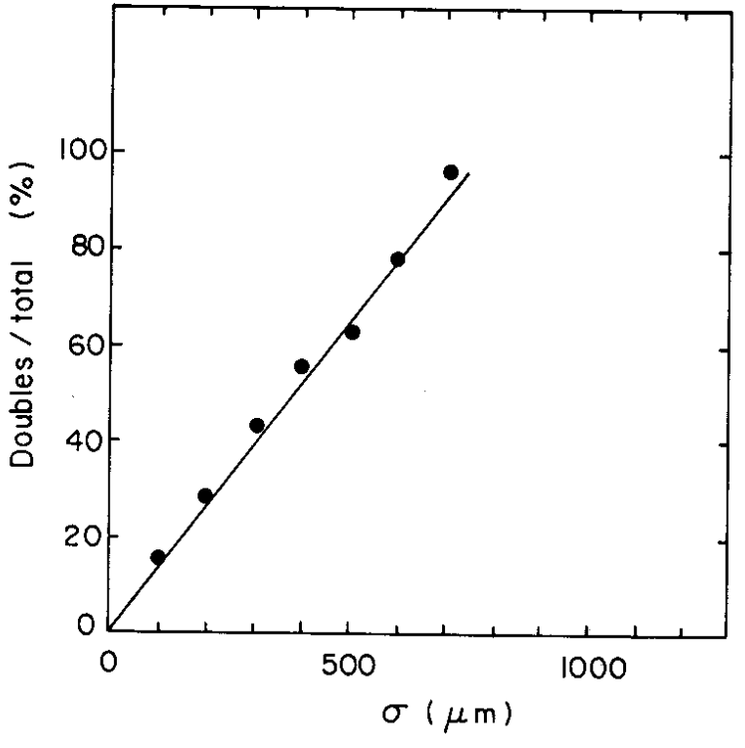
Doubles / total (%)
100
80
60
40
20
0
0
500
1000
σ (μm)

Fig. 28

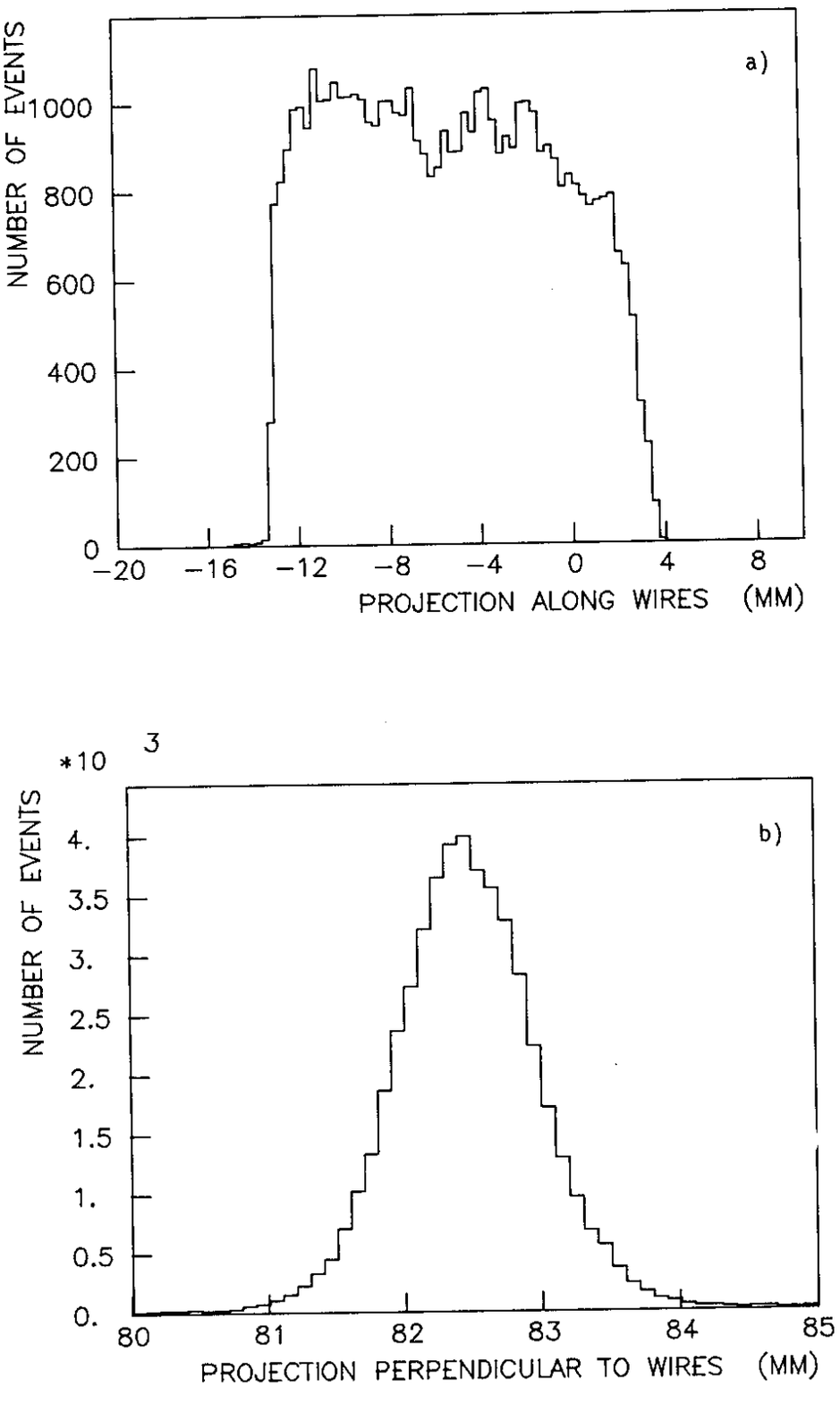
a)
NUMBER OF EVENTS
1000
800
600
400
200
0
−20
−16
−12
−8
−4
0
4
8
PROJECTION ALONG WIRES (MM)
b)
*10 3
NUMBER OF EVENTS
4.
3.5
3.
2.5
2.
1.5
1.
0.5
0.
80
81
82
83
84
85
PROJECTION PERPENDICULAR TO WIRES (MM)

Fig. 29

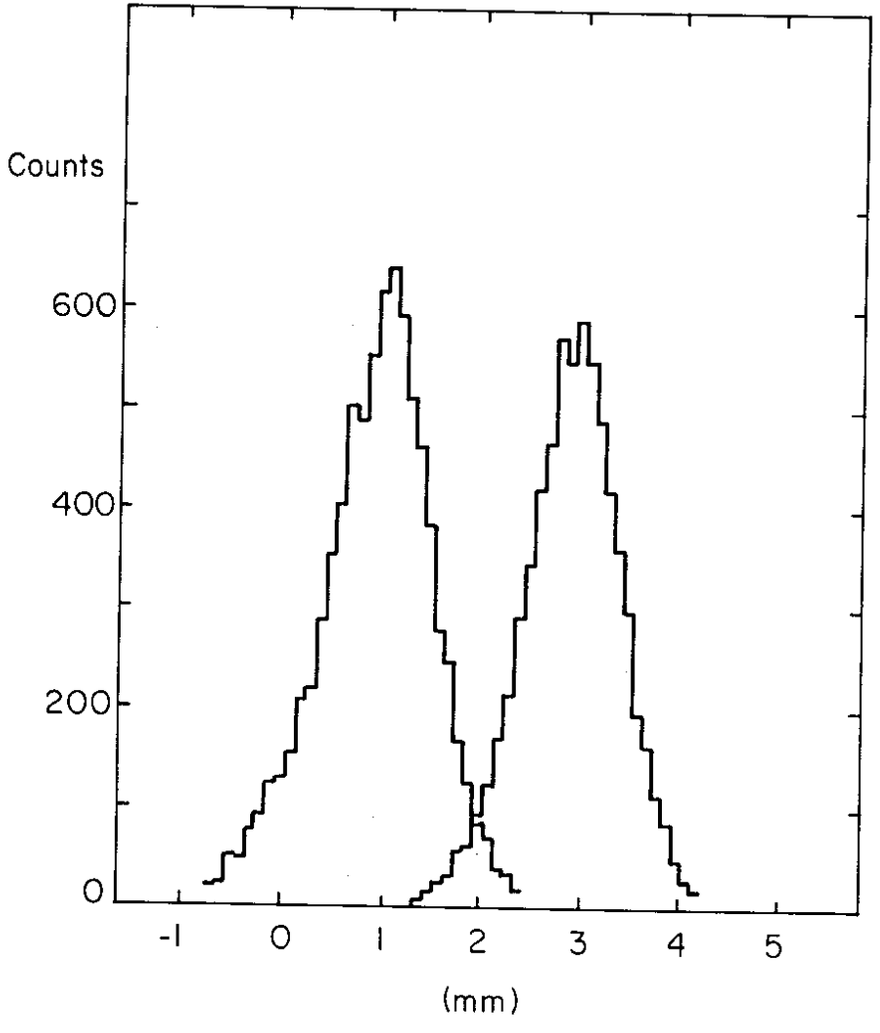
Counts
600
400
200
0
-1
0
1
2
3
4
5
(mm)

Fig. 30

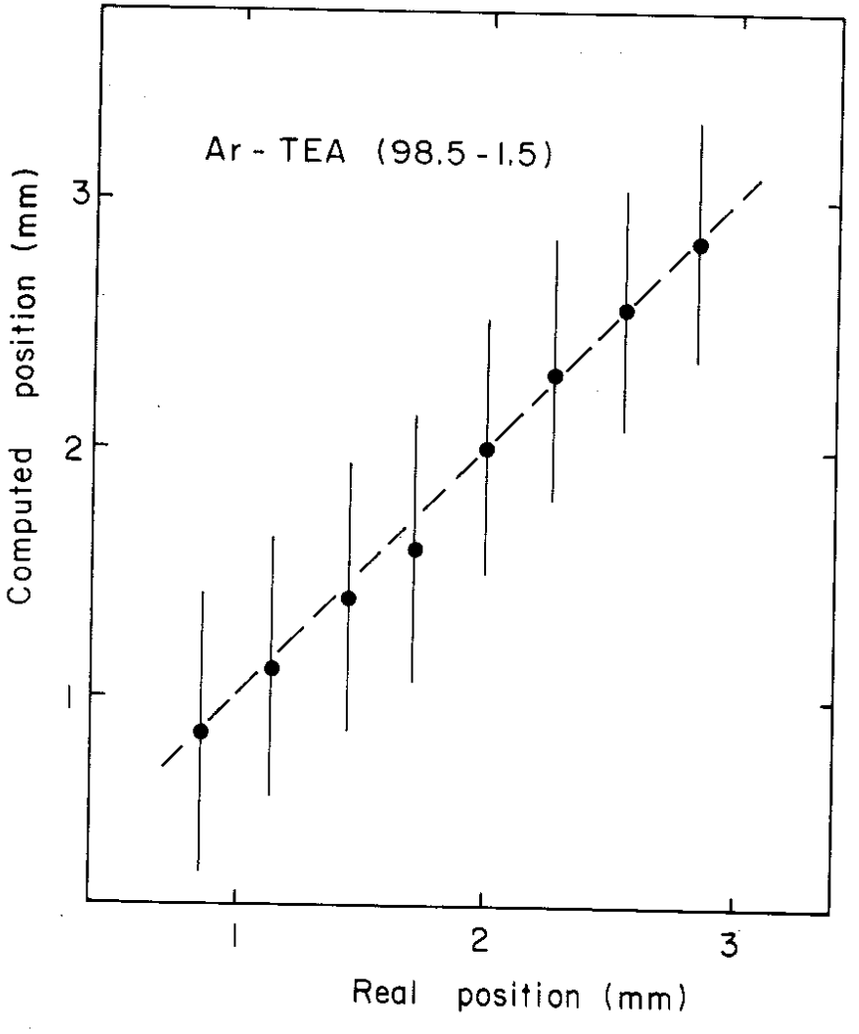
Ar - TEA (98.5 - 1.5)
Computed position (mm)
1
2
3
1
2
3
Real position (mm)

Fig. 31

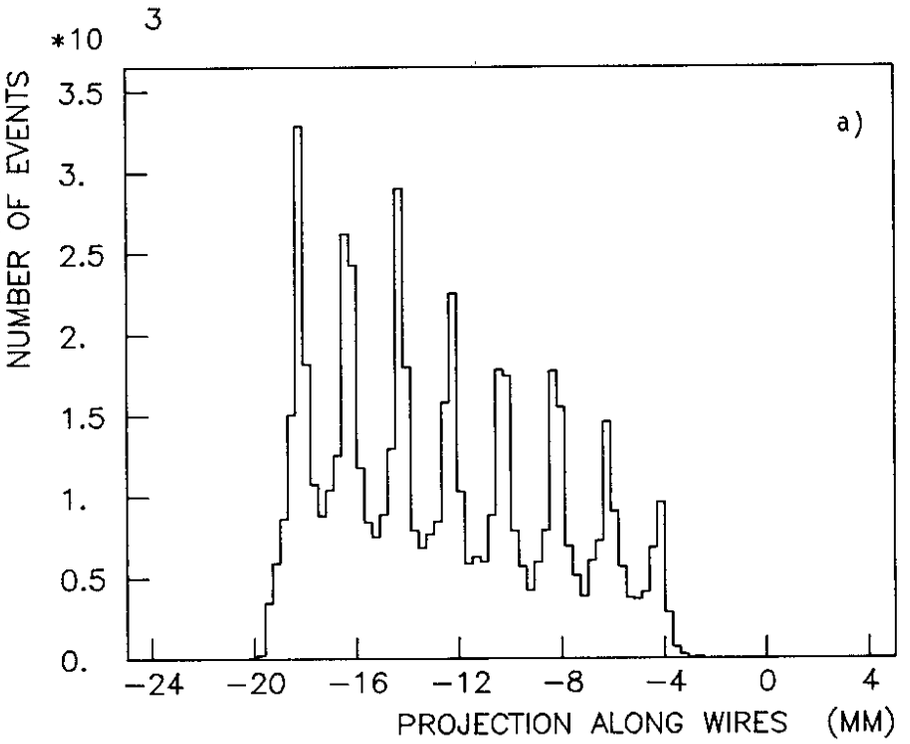
*10 3
NUMBER OF EVENTS
3.5
3.
2.5
2.
1.5
1.
0.5
0.
a)
−24
−20
−16
−12
−8
−4
0
4
PROJECTION ALONG WIRES (MM)

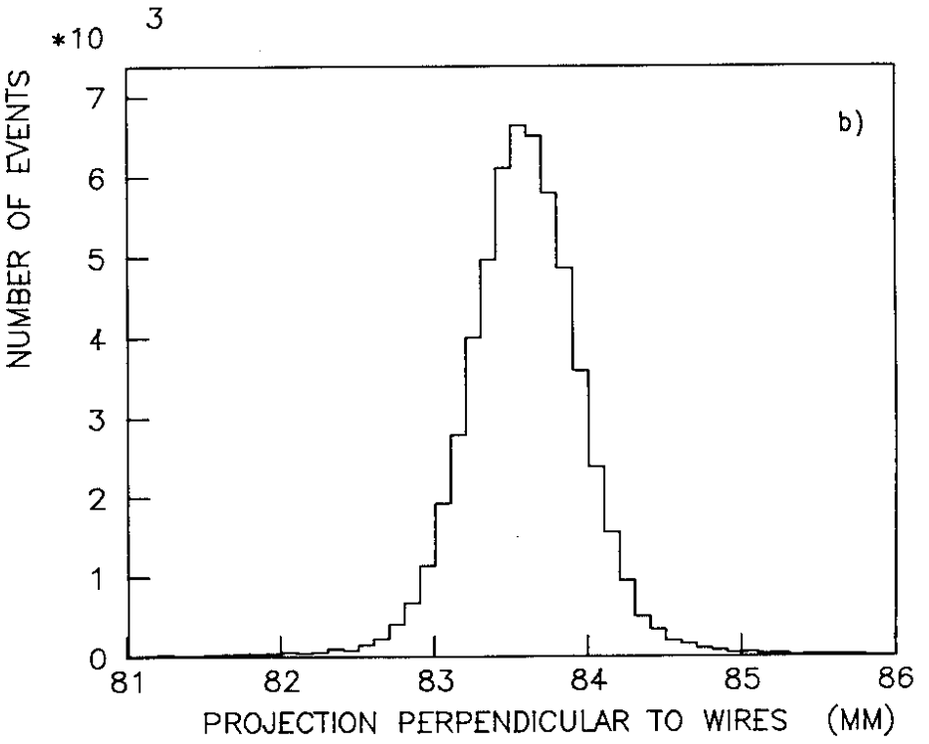
*10 3
NUMBER OF EVENTS
7
6
5
4
3
2
1
0
b)
81
82
83
84
85
86
PROJECTION PERPENDICULAR TO WIRES (MM)

Fig. 32

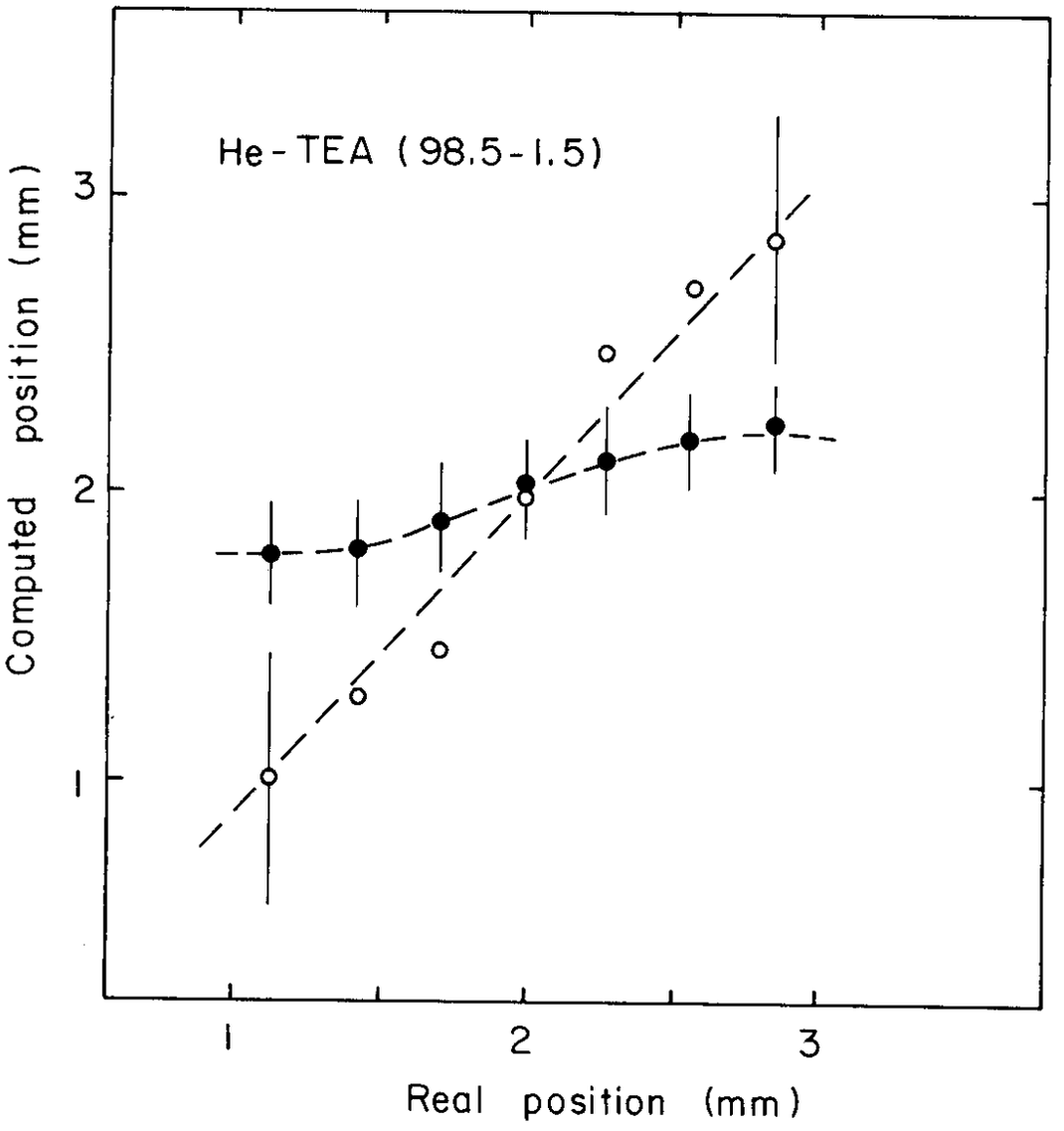


Fig. 33